

SÍGAME V3: GAS FRAGMENTATION IN POST-PROCESSING OF COSMOLOGICAL SIMULATIONS FOR MORE ACCURATE INFRARED LINE EMISSION MODELING

KAREN PARDOS OLSEN,¹ BLAKESLEY BURKHART,^{2,3} MORDECAI-MARK MAC LOW,^{4,3} ROBIN G. TRESS,⁵
THOMAS R. GREVE,^{6,7,8} DAVID VIZGAN,⁹ JAY MOTKA,¹ JOSH BORROW,¹⁰ GERGÖ POPPING,¹¹ ROMEEL DAVÉ,^{12,13,14}
ROWAN J. SMITH,¹⁵ AND DESIKA NARAYANAN^{16,17,6}

¹*Department of Astronomy and Steward Observatory, University of Arizona, Tucson, AZ 85721, USA*

²*Department of Physics and Astronomy, Rutgers, The State University of New Jersey, 136 Frelinghuysen Rd, Piscataway, NJ 08854, USA*

³*Center for Computational Astrophysics, Flatiron Institute, 162 Fifth Avenue, New York, NY 10010, USA*

⁴*Department of Astrophysics, American Museum of Natural History, New York, NY 10024, USA*

⁵*Universität Heidelberg, Zentrum für Astronomie, Institut für theoretische Astrophysik, Albert-Ueberle-Str. 2, 69120 Heidelberg, Germany*

⁶*Cosmic Dawn Center (DAWN)*

⁷*DTU-Space, Technical University of Denmark, Elektrovej 327, DK-2800 Kgs. Lyngby, Denmark*

⁸*Dept. of Physics & Astronomy, University College London, Gower Place, WC1E 6BT London*

⁹*Department of Astronomy, Wesleyan University, Middletown, CT 06457, USA*

¹⁰*Institute for Computational Cosmology, Department of Physics, University of Durham, South Road, Durham DH1 3LE, UK*

¹¹*European Southern Observatory, 85478 Garching bei München, Germany*

¹²*Institute for Astronomy, Royal Observatory, Univ. of Edinburgh, Edinburgh EH9 3HJ, UK*

¹³*Department of Physics and Astronomy, University of the Western Cape, Robert Sobukwe Road, Bellville 7535, South Africa*

¹⁴*South African Astronomical Observatories, Observatory, Cape Town 7925, South Africa*

¹⁵*Jodrell Bank Centre for Astrophysics, University of Manchester, Oxford Road, Manchester M13 9PL, UK*

¹⁶*Department of Astronomy, University of Florida, 211 Bryant Space Sciences Center, Gainesville, FL 32611 USA*

¹⁷*University of Florida Informatics Institute, 432 Newell Drive, CISE Bldg E251, Gainesville, FL 32611*

Submitted to ApJ

ABSTRACT

We present an update to the framework called SImulator of GALaxy Millimeter/submillimeter Emission (SÍGAME). SÍGAME derives line emission in the far-infrared (FIR) for galaxies in particle-based cosmological hydrodynamics simulations by applying radiative transfer and physics recipes via a post-processing step after completion of the simulation. In this version, a new technique is developed to model higher gas densities by parametrizing the gas density probability distribution function (PDF) in higher resolution simulations for use as a look-up table, allowing for more adaptive PDFs than in previous work. SÍGAME v3 is tested on redshift $z = 0$ galaxies drawn from the SIMBA cosmological simulation for eight FIR emission lines tracing vastly different interstellar medium phases. Including dust radiative transfer with SKIRT and high resolution photo-ionization models with CLOUDY, this new method is able to self-consistently reproduce observed relations between line luminosity and star formation rate in all cases, except for [N II]122, [N II]205 and [O I]63, the luminosities of which are overestimated by median factors of 1.6, 1.2 and 1.2 dex, respectively. We attribute the remaining disagreement with observations to the lack of precise attenuation of the interstellar light on subgrid scales ($\lesssim 200$ pc).

Keywords: galaxies, ISM, simulation, modeling, radiative transfer

1. INTRODUCTION

The physical and chemical state of the interstellar medium (ISM) plays a key role in determining the star formation rate (SFR) of a galaxy and is therefore of immense importance for understanding galaxy evolution.

Macroscopic galactic events like starbursts and mergers create pressure and density waves that determine where and how the giant molecular clouds (GMCs) form in which stars and planets grow (e.g. Colombo et al. 2014; Sun et al. 2018; Chevance et al. 2020; Alves et al. 2020).

Resolved observations of nearby clouds and detailed simulations that track individual cores in GMCs from initial perturbations to final collapse, can probe the actual density distribution above the highest density achievable in cosmological simulations. Both observations and numerical work to this effect have determined that the dense gas in molecular clouds (with extinctions $A_v > 1$ and/or $n > 10^3 \text{ cm}^{-3}$) typically has a density PDF with a power-law tail at the high end set by gravitational collapse (Klessen 2000; Kainulainen et al. 2009; Collins et al. 2012; Girichidis et al. 2014; Burkhardt et al. 2015; Schneider et al. 2015; Lombardi et al. 2015; Burkhardt et al. 2017; Mocz et al. 2017; Padoan et al. 2017; Chen et al. 2018; Alves et al. 2017). The low density portion of the density probability density function (PDF) might follow a log-normal shape but this is highly uncertain due to selection effects, completeness, and the influence of stellar feedback (Alves et al. 2017; Chen et al. 2018).

On galactic scales, it becomes too computationally expensive for simulations to model the fragmentation and collapse of each cloud, not to mention the subsequent stellar feedback processes. Instead, parametrizations are used as for example in the cosmological simulations SIMBA (Davé et al. 2019) and IllustrisTNG (Weinberger et al. 2017; Pillepich et al. 2018). In SIMBA, an H_2 -based SFR recipe is used where the amount of H_2 is estimated from the metallicity and local column density following the sub-grid model of Krumholz & Gnedin (2011). In IllustrisTNG, gas with density $n \gtrsim 0.1 \text{ cm}^{-3}$ is allowed to form stars in accordance with the empirically defined Kennicutt-Schmidt relation. Both simulations lack the resolution to track individual stars, and instead assume a Chabrier (2003) initial mass function for stellar populations formed.

Synthetic observations of simulated galaxies are our most promising way of directly comparing models with observations of the ISM. Observations of the ISM typically target its most effective cooling channels, namely far-infrared (FIR) emission lines. These were discovered by the Kuiper Airborne Observatory (Watson et al. 1984; Stacey et al. 1991; Lord et al. 1996). The subsequent *Infrared Space Telescope* (Kessler et al. 1996) and *Herschel Space Observatory* (*Herschel* hereafter; Pilbratt et al. 2010) showed that the strongest emission lines come from a handful of species, namely neutral and ionized oxygen, singly ionized carbon, ionized nitrogen

as well as molecular lines such as the CO rotational lines. Together, these species probe all phases of the ISM from GMCs to photon-dominated regions (or photodissociation regions; PDRs), warm neutral medium and hot ionized gas. Existing telescopes like ALMA, NOEMA and SOFIA as well as upcoming space and balloon missions (e.g. GUSTO and ASTHROS) provide an ever-growing database of emission line observations of galaxies at all redshifts, requiring detailed modeling of the same lines for their correct interpretation. By taking a snapshot of a hydrodynamic simulation containing gas, stars and dark matter, line emission can be calculated as a post-processing step for each cell or particle in the simulation using physically motivated recipes.

All efforts to simulate emission lines have had to determine small-scale values for: 1) the structure and local spectral shape of the radiation field, in particular in the far-ultraviolet (FUV), 2) the structure of gas density, and 3) the local chemistry and level populations. Due to computational constraints, most of these are not calculated with enough precision in the simulation itself, and must hence be derived in post-processing based on sub-grid models. Below, we summarize the current approaches:

1. For the FUV, the current practice typically involves adopting the solar neighborhood FUV interstellar radiation field strength G_0 (Habing 1968) and scaling it by the global SFR of the simulated galaxy compared to that of the Milky Way (e.g. Vallini et al. 2019) to get a galaxy-averaged FUV flux; or by using the local SFR density to get a local kpc-scale FUV flux (e.g. Olsen et al. 2017; Popping et al. 2019). Pallottini et al. (2019) demonstrated the use of on-the-fly radiative transfer for a high-resolution adaptive mesh refinement simulation of a $z \sim 6$ galaxy, and some large cosmological simulations have now also seen on-the-fly radiative transfer, albeit only from Big Bang through the epoch of reionization and not down to low redshifts (Ocvirk et al. 2016; Wu et al. 2019; Ocvirk et al. 2020). *In this work, we introduce a post-processing radiative transfer calculation for large-box simulations at $z = 0$*
2. Retrieving the high density ($n > 10^4 \text{ cm}^{-3}$) gas during post-processing of a cosmological simulation is crucial to model several FIR lines, as can be seen from the critical densities of typical FIR lines listed in Table 1. This step is typically done by adopting a clumping factor that artificially increases the H_2 production (e.g. Narayanan et al. 2008; Gnedin et al. 2009; Davé et al. 2016; Lupi &

Bovino 2020), adopting a locally observed molecular cloud mass spectrum together with a derived cloud radius and assumed inner density profile (e.g. Olsen et al. 2015, 2016, 2017; Popping et al. 2019; Inoue et al. 2020), or fragmenting the gas on sub-grid scales following a log-normal density PDF as motivated by Padoan & Nordlund (2011) for isothermal molecular clouds, using a fixed Mach number (Vallini et al. 2019; Leroy et al. 2017) or calculating the Mach number from local gas properties (e.g. Narayanan & Krumholz 2014; Pallottini et al. 2019). However, the use of the lognormal PDF may be physically unmotivated as evidenced by the log-normal+power-law PDF seen in observations and simulations, as described earlier. *In this work, we employ simulations of higher spatial resolution as look-up tables and use analytic relations of density PDFs from Burkhart (2018) to infer the PDF on sub-grid scales in a cosmological simulation.*

3. Once the radiation field and density are determined, there are many tools publicly available that simultaneously solve for ionization state, temperature and line excitation, with some of them being tailored to a specific ISM phase. For an overview of widely used tools to solve for the chemistry and generate line emission in the ISM, see Olsen et al. (2018), which also discusses the limitations of each approach. *In this work, we use the photoionization code CLOUDY (Ferland et al. 2017) to set the shape of the spectrum locally as well as calculate chemistry and line emission.*

As previously mentioned, in addition to inferring the PDF in higher resolution simulations as described in point 2 above, we also use a theoretical framework to estimate the amount of self-gravitating gas not resolved in the galaxy-sized simulation. In order to alleviate tensions with observations and dense gas models that use a log-normal PDF, Burkhart & Mocz (2019) derive a dense gas and star formation model based primarily on the presence of a power law tail. The work provides an analytic expression connecting the transitional column density value between log-normal and power-law to the width and of the log-normal and the slope of the power-law which we will use here (see also Collins et al. 2012; Burkhart et al. 2017; Burkhart 2018).

With this paper, we present a new version of our post-processing framework Simulator of Galaxy Millimeter/submillimeter Emission (SÍGAME; Olsen et al. 2017) to model FIR/mm line emission in particle-based hydrodynamic simulations, and test it on a large sample

Table 1. Critical densities of important ISM cooling lines in the FIR. CO critical densities were calculated using the spontaneous emission coefficients from the LAMDA database as accessed on 21 Aug 2020 (Schöier et al. 2005), using a temperature of 100 K and typical collision cross section of 10^{-15} cm^{-3} . The [C II] critical densities are from Goldsmith et al. (2012), calculated at a temperature of 500 K. The remaining critical densities are from Madden et al. (2013) at 300 K.

Line	$n_{crit} \text{ (cm}^{-3}\text{)}$	Origin
[C II]	$16^a, 2.4 \times 10^3^b, 4.8 \times 10^3^c$	All ISM, but mainly PDRs
[O I]63	$4.7 \times 10^5^b$	PDRs
[O III]88	510^a	H II regions, radiation dominated by OB stars
[N II]122	310^a	Ionized ISM
[N II]205	48^a	Ionized ISM
CO(1-0)	650^c	Molecular ISM
CO(2-1)	$6.2 \times 10^3^c$	Molecular ISM
CO(3-2)	$2.2 \times 10^4^c$	Molecular ISM

^aFor collisions with electrons.

^bFor collisions with hydrogen atoms.

^cFor collisions with H2 molecules.

of emission lines for comparison with observations. Section 2 gives a quick overview of the new structure of SÍGAME and lists the updates made since the previous version. The test sample of galaxies used for the tests are described in Section 3. Section 4 provides more details on the steps that SÍGAME goes through. Section 5 compares and validates the code by comparison with observations and the previous version of SÍGAME. Finally, Section 6 discusses the results and provides caveats for using this method and we conclude in Section 7.

Throughout this paper, we adopt a flat cold dark matter cosmology with cosmological parameters $\Omega_\Lambda = 0.693$, $\Omega_m = 0.307$, $\Omega_b = 0.048$, and dimensionless Hubble parameter $h = 0.678$ (Planck Collaboration et al. 2016).

2. SÍGAME VERSION 3 OVERVIEW

SÍGAME derives FIR/mm line emission of simulated galaxies by post-processing a particle-based cosmological hydrodynamics simulation. Figure 1 provides a quick look at the overall structure of SÍGAME version 3. This section will summarize the updates made since the last version of the code, with more details below (Sect. 4).

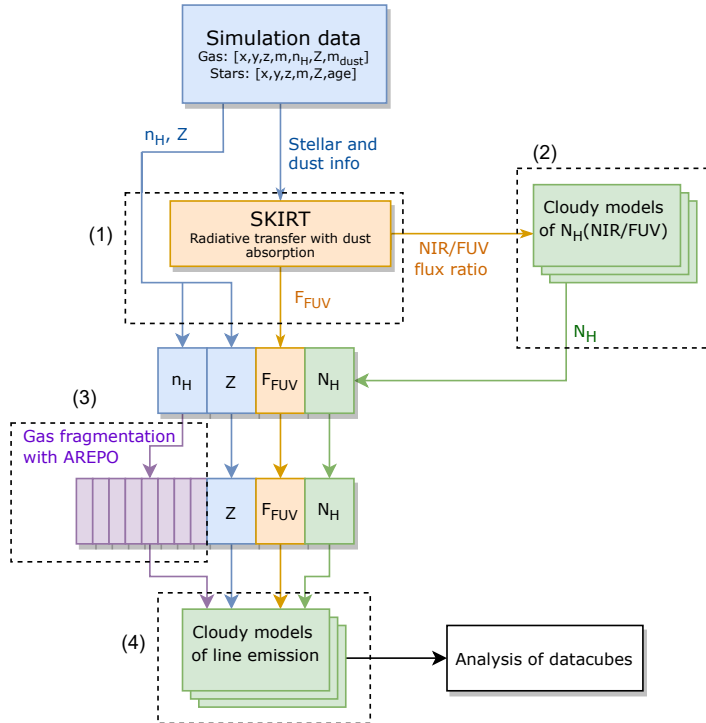


Figure 1. Flow chart illustrating the structure of SIGAME v3.

2.1. Main updates

Leung et al. (2020) adapted version 2 of *síGAME* to apply it to the SIMBA simulation for the first time to study the [C II] luminosity function at $z = 6$. With this version 3, the main updates are:

- Radiative transfer of stellar FUV emission through dust: *síGAME* v2 used a library of STARBURST99 (Leitherer et al. 2014) synthesis models for stellar populations to derive the local FUV field, without taking into account the potentially important effect of dust absorption. In *síGAME* v3 a full dust radiative transfer calculation is performed using the three-dimensional (3D) radiative transfer code SKIRT¹ (Camps & Baes 2020) and the actual dust-to-metal ratios from the SIMBA simulation (Li et al. 2019).
- Fragmentation of the gas on sub-grid scales: In previous versions of *síGAME*, gas particles from cosmological simulations were divided into a diffuse and a dense gas phase, the latter being further divided into spherical GMC-like structures with masses $> 10^4 M_{\odot}$. With the new version of *síGAME*, gas particles are first distributed on an

adaptive grid with SKIRT and then fragmented according to the local gas and SFR volume densities using the output from a high resolution simulation, and thereby avoiding the assumption of spherical clouds.

- High resolution thermo-chemistry of the ISM: As in previous versions of *síGAME*, we use the photoionization code CLOUDY (this time version 17.02) to calculate the chemical and thermal state of the gas and the resulting line emission. However, because of the decision to fragment the gas to smaller mass and size scales, we have moved to using the GRID COMMAND feature of CLOUDY, allowing for a look-up table of higher resolution.

3. THE $z = 0$ GALAXY SAMPLE

We apply *síGAME* to a simulated galaxy sample from the SIMBA cosmological galaxy formation simulation (Davé et al. 2019). The SIMBA simulations are run using the meshless finite mass hydrodynamics technique in the GIZMO N-body plus hydrodynamics code (Hopkins 2015, 2017). The main SIMBA run evolves 1024^3 gas elements and 1024^3 dark matter particles within a $100h^{-1}$ Mpc volume (SIMBA-100) from $z = 249 \rightarrow 0$. To improve the dynamic range and test resolution convergence, we also use a higher-resolution run with 512^3 gas elements and

¹ <http://www.skirt.ugent.be/>

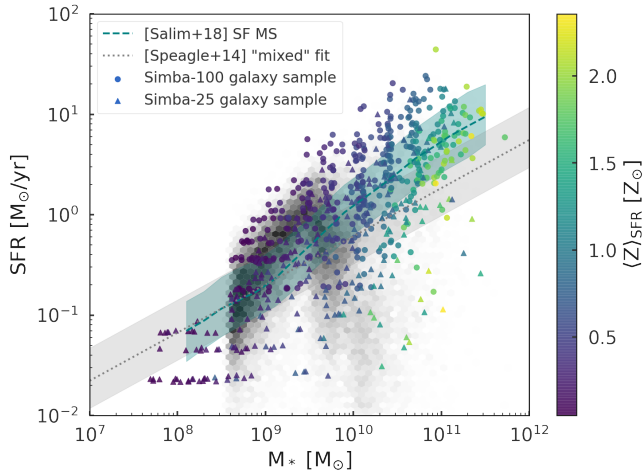


Figure 2. The position on the SFR-stellar mass plane of the selected test sample at $z = 0$ of 400 SIMBA-100 galaxies (circles) and 240 SIMBA-25 galaxies (triangles), with both samples color-coded by SFR-weighted metallicity. For comparison, the grey hexbin contours show the overall distribution of $z = 0$ star-forming galaxies in SIMBA-100 after discarding galaxies with no star formation according to CAESAR or fewer than 300 gas particles. The observed $z = 0$ main sequence from two studies are also shown (Salim et al. 2018; Speagle et al. 2014) with shaded regions referring to 16th and 84th percentiles in the case of Salim et al. (2018) and 0.2 dex for Speagle et al. (2014).

512^3 dark matter particles within a $25h^{-1}$ Mpc volume (SIMBA-25).

SIMBA includes a range of sub-grid models for galaxy formation physics, including H_2 -based star formation, two-phase kinetic galactic winds, torque-limited and Bondi black hole accretion, three types of AGN feedback, and a sub-grid model to form and destroy dust during the simulation run (Li et al. 2018, 2019). The galaxy properties in SIMBA have been compared to various observations across cosmic time and shown to provide reasonable agreement (e.g. Thomas et al. 2019; Appleby et al. 2020; Lower et al. 2020; Rodríguez Montero et al. 2019). For more details we refer to Davé et al. (2019).

We extracted samples of galaxies from the $z = 0$ snapshots of SIMBA-100 and SIMBA-25 using the CAESAR galaxy and halo catalog generator, which identifies galaxies using a six-dimensional friends-of-friends algorithm applied to dense gas ($n > 0.13 \text{ cm}^{-3}$) and stars (Thompson 2015). Before making any selection cuts, a total of 20,428 and 2,463 galaxies were found by CAESAR for SIMBA-100 and SIMBA-25, respectively. To ensure we have a reasonably well-resolved gas distribution within the galaxy, we only consider galaxies with > 300 gas el-

ements in both simulation boxes, corresponding to a gas mass of at least $5.6 \times 10^9 M_\odot$ and $0.7 \times 10^9 M_\odot$ in SIMBA-100 and SIMBA-25, respectively. From these we select a test sample of 400 galaxies from SIMBA-100 and another sample of 240 galaxies from SIMBA-25. The samples were selected to span a wide range in stellar mass, SFR and gas mass. Only galaxies found to have non-zero mean SFR over the past 100 Myr were included.

Figure 2 shows the positions of the SIMBA-100 galaxy sample in the SFR- M_* space. The distribution of all 16,617 SIMBA-100 $z = 0$ galaxies identified with CAESAR and having non-zero mean SFRs is shown underneath with hexbin contours. The agreement with observations by Salim et al. (2018) is generally good, though SIMBA overestimates the SFR over the range $M_* \sim 10^{9.5} - 10^{10} M_\odot$ (see discussion of this in Davé et al. 2019). Overall, SIMBA reproduces the observed SFR- M_* distribution fairly well, both in terms of the main sequence and the quenched fractions (Davé et al. 2019), as well as the bimodality in specific SFR (Katsianis et al. 2020).

For our sample of 400 galaxies, hydrogen densities range from 0.5 to 66 cm^{-3} and SFR-weighted mean metallicities $\langle Z \rangle_{\text{SFR}}$ span 0.1 to $2.4 Z_\odot$. By weighing the metallicity by SFR, we are approximating the metallicity that would be observed using nebular emission lines since these lines primarily trace star-forming regions. Global galaxy properties such as stellar mass, gas mass, SFR, $\langle Z \rangle_{\text{SFR}}$, and radius can be found in Table 4 together with their line luminosities in Table 5 in Appendix A and online.

We note that the version of SÍGAME as presented in this paper is set up to take the snapshot information from SIMBA. In the near future, we plan to adapt the code so that it can also accept output from higher resolution, non-cosmological, zoom particle-based, as well as mesh-based simulations, but for the purpose of testing the new version, we use the cosmological particle-based format to which SÍGAME has previously been applied.

4. SÍGAME V3

The new SÍGAME framework consists of four major steps, each indicated on Figure 1 with numbered boxes. The following four subsections describe the algorithms that are applied within each step.

4.1. Dust attenuation with SKIRT (step 1)

Figure 3 illustrates the outcome of modeling and propagating the stellar light with the 3D radiative transfer code SKIRT (Camps & Baes 2020). SKIRT requires information on the dust and stellar distribution, most of which can be extracted from the SIMBA snapshots themselves. SKIRT then employs the Monte Carlo tech-

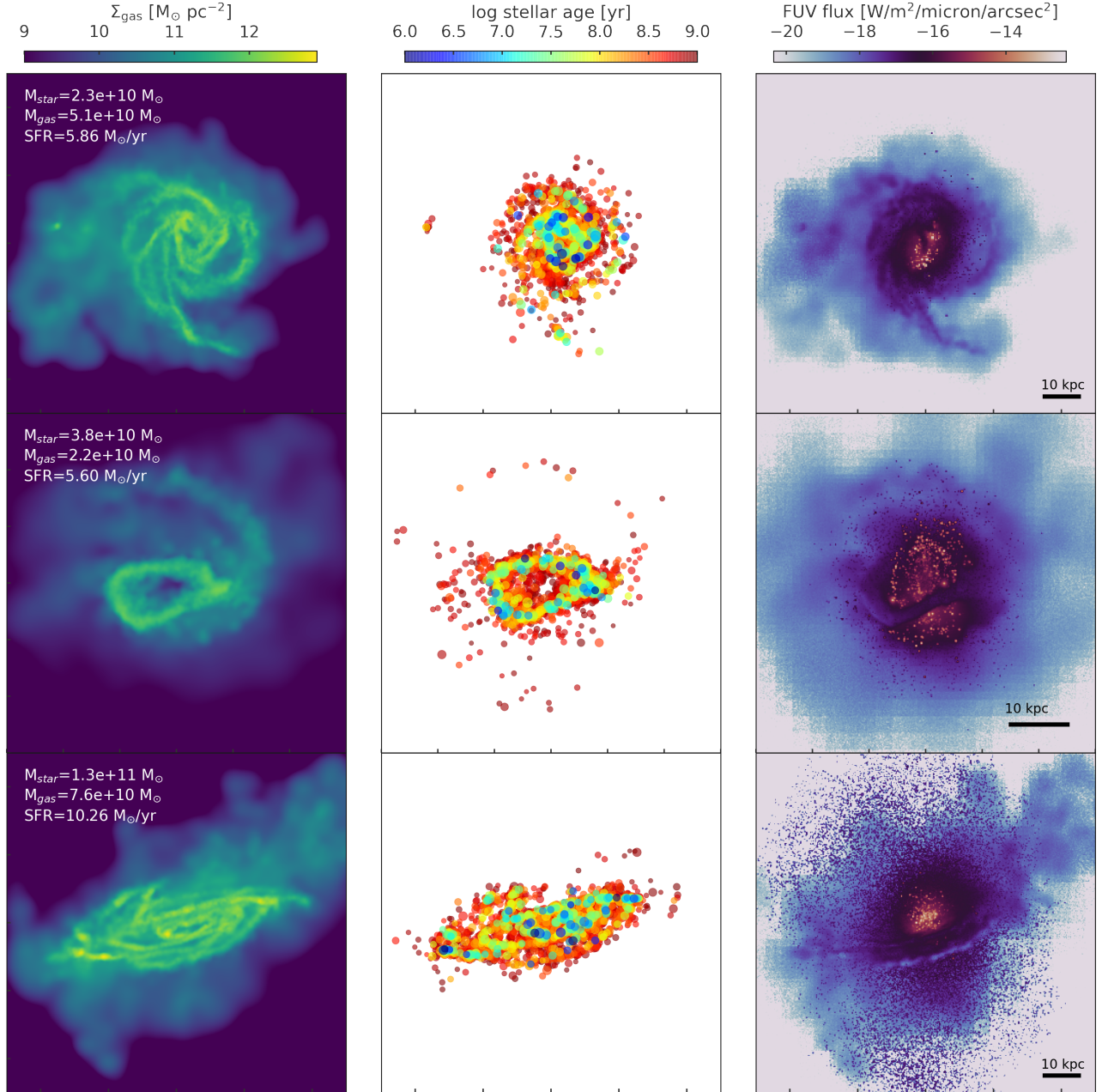


Figure 3. Examples of three SIMBA-25 galaxies going through step 1 of SÍGAME, where stellar light is propagated, attenuated and re-emitted by dust grains using the radiative transfer code SKIRT. *Left column:* Surface density maps of the total gas mass in SIMBA. *Center column:* Positions and ages of all stellar population particles with ages below 1 Gyr. The sizes of the stellar circles scale with stellar population mass. *Right column:* Maps of observed FUV (6–13.6 eV) flux derived with SKIRT as observed from a distance of 10 Mpc, showing increased FUV flux in areas close to young stellar populations and attenuation by regions of dense gas.

nique to emulate the relevant physical processes including scattering, absorption, and emission of photons as they pass through the interstellar dust. For the purposes of this paper, we found that a total of 10^8 photons per galaxy was enough to give stable results. See Appendix B for a test increasing the number of photon packets to 10^9 that resulted in a negligible change in total FUV luminosity and FUV flux distribution. In the following, we provide more detail on the specific input parameters used for and the operation of SKIRT.

For the dust component (“MediumSystem” in SKIRT), we directly use the dust masses that are calculated on-the-fly in SIMBA (Li et al. 2019). For the dust types and composition, we use the built-in THEMIS model (Jones et al. 2017) for dust in the diffuse interstellar medium that can be invoked in SKIRT. This dust mixture contains two families of dust particles; amorphous silicate and amorphous hydrocarbon (we refer to Jones et al. 2017 for more detail).

For the stellar component (“SourceSystem” in SKIRT), we adopt a Chabrier (2003) IMF as also used in SIMBA. A smoothing length for each stellar particle must be provided to SKIRT, but as SIMBA lacks this parameter, we assumed a smoothing length that scales linearly with stellar mass and spans 100 to 300 pc. We note that the exact smoothing length prescription for the stars has little effect on the final flux distribution. Finally, SKIRT requires the initial mass of each stellar particle and not the current stellar mass as reported in the output from SIMBA, since the spectral energy distributions used by SKIRT already take into account the mass evolution of the population based on its age and metallicity. The initial stellar mass, before mass loss due to stellar evolution, is calculated using the publicly available Python-FSPS code, which itself is a python translation of the Flexible Stellar Population Synthesis code, in order to convert current stellar mass and formation time into initial stellar masses (Conroy et al. 2009; Conroy & Gunn 2010; Foreman-Mackey et al. 2014).

The resulting total infrared (3–1100 μm) luminosities span from $2.41 \times 10^7 L_{\odot}$ to $2.73 \times 10^{11} L_{\odot}$ and FUV (6–13.6 eV) luminosities from $5.78 \times 10^7 L_{\odot}$ to $1.09 \times 10^{10} L_{\odot}$ using the SIMBA-100 dust masses directly. The post-processing with SKIRT returns a spectrum for each cell of each galaxy on an oct-tree adaptive grid. The rest of SÍGAME works on this grid structure, for which gas densities are calculated with the SWIFTSIMIO package (Borrow & Borrisov 2020), and metallicity, dust-to-mass (DTM) ratio, element abundances, and SFR volume density are inherited from the nearest fluid element in the SIMBA simulation.

4.2. Attenuation by intervening gas with CLOUDY (step 2)

In addition to being attenuated by dust grains, interstellar light from stars is also absorbed by gas, in particular in the hydrogen-ionizing regime at photon energies above 13.6 eV. With SKIRT a spectrum is generated in each cell that has been attenuated by dust only, which tends to absorb radiation in the FUV at 6–13.6 eV (Gnedin et al. 2008). In order to account for the additional attenuation by gas, we run a suite of CLOUDY models over a range of total hydrogen column densities, keeping the metallicity at $1 Z_{\odot}$ and maintaining the dust size distribution and abundance to that appropriate for the ISM of the Milky Way as given by the CLOUDY “grains ISM” command. The latter includes both a graphitic and silicate component and generally reproduces the observed overall extinction properties for a ratio of extinction per reddening of $RV \equiv A_V/E(B-V) = 3.1$ (we refer to the CLOUDY manual for details). We use the local ISM abundance table of CLOUDY, which is a mean of the warm and cold phases of the ISM from Cowie & Songaila (1986) and Savage & Sembach (1996). In these CLOUDY models, and all other CLOUDY models in this work, the CMB at $z = 0$ is included as an additional blackbody radiation field. For the incident continuum, the local ISRF in CLOUDY is used. The resulting transmitted spectra are shown in Figure 4. The spectrum is not attenuated significantly for column densities below around 10^{18} cm^{-2} , and above this column density the incident spectra are attenuated both above and below 13.6 eV.

From the shape of the spectra in Figure 4, we calculate the slope at energies below 13.6 eV in the spectra and link it to the column density of each model. To quantify the slope, we calculate the ratio between near-infrared flux (0.5–2 eV) and FUV flux (red and teal shaded regions in Fig. 4). The NIR-to-FUV flux ratio starts to increase significantly at gas column densities $N_{\text{H}} > 10^{19} \text{ cm}^{-2}$. Assuming that the attenuation in the NIR-to-FUV flux ratio is primarily due to dust, we can now match the derived NIR/FUV flux ratio with that of SKIRT in each simulation cell to translate the dust extinction into a column density of gas that the stellar light has passed through. This method comes with two approximations: 1) it assumes a constant DTM ratio, which is inconsistent with SIMBA where dust abundances are tracked separately, 2) it requires the metallicity of the intervening gas, but since we do not know the exact path of each photon, we fix the metallicity to solar. The mass-weighted metallicities of our model galaxies range from 0.03 to $0.74 Z_{\odot}$ (SFR-weighted from 0.1 to $1.9 Z_{\odot}$), so we believe this to be a reasonable approximation.

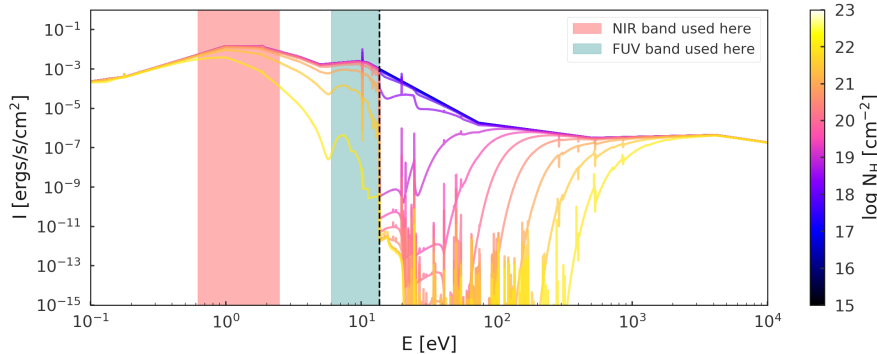


Figure 4. Transmitted spectra for a set of CLOUDY models with hydrogen density 1 cm^{-3} , solar dust and metallicity abundances and a range in total hydrogen column density shown in different colors. The NIR and FUV photometric bands that we use are indicated with shaded regions and a vertical dashed line highlights the 13.6 eV ionization potential of hydrogen. Significant attenuation only occurs at column densities $N_{\text{H}} > 10^{17.5} \text{ cm}^{-2}$. Below that value the spectra become indistinguishable from the input spectrum.

4.3. Gas fragmentation (step 3)

Due to the limited resolution of cosmological simulations, the individual cells do not contain densities higher than $\sim 10 \text{ cm}^{-3}$ (see Appendix C). However all the FIR emission lines considered here can or will only be excited at much higher densities, as can be seen from the critical densities listed in Table 1. All high density clumps and filaments on scales below the typical minimum smoothing scale of $\sim 1 \text{ kpc}$ in the SIMBA galaxies are unresolved. In order to perform the dust radiative transfer, SKIRT introduces cells of smaller sizes, with cell sizes ranging from 19 pc to 6.3 kpc (for the SIMBA-100 galaxies) and a mass-weighted distribution in cell sizes that peaks at $\sim 200 \text{ pc}$, but this procedure does not increase the density of the gas.

To mitigate the lack of resolution in density, this version of SÍGAME turns towards simulations made at much higher spatial resolution in order to use them as look-up tables that can help describe the fragmentation of the gas on sub-grid scales. The high-resolution data set chosen comes from a simulation performed with the moving-mesh code AREPO (Springel 2010) of an interacting M51-like galaxy model (Tress et al. 2020). The simulation (hereafter described as AREPO-M51) reached sub-parsec resolution in dense gas and allowed for an analysis of the formation and destruction of GMCs and how the evolution of GMCs depends only weakly on galaxy-galaxy interactions.

4.3.1. The AREPO-M51 simulation

For details on the simulation setup we refer to Tress et al. (2020), summarizing here only the components of relevance to this project. The AREPO-M51 simulation was designed to be able to resolve and study GMCs in the context of a galaxy interaction. The simula-

tion setup includes a time-dependent, non-equilibrium, chemistry network tracking hydrogen and CO chemistry, and follows star formation and feedback processes reaching sub-parsec resolutions at densities $n \gtrsim 100 \text{ cm}^{-3}$ (see Fig. 3 of Tress et al. 2020). The calculations were executed using AREPO, a moving-mesh magnetohydrodynamic (MHD) code coupled to an oct-tree gravity solver, from which only the hydrodynamic capabilities were used (Weinberger et al. 2020). At each time-step the code constructs the Voronoi grid given a set of mesh generating points that are constrained to move following the local velocity of the fluid. This pseudo-Lagrangian moving-mesh technique is naturally adaptive, allowing for high dynamic range in spatial scales down to the substructure of GMCs.

The galaxy model and the interaction with a companion were adjusted to resemble the M51 system and the chemical network followed the cooling and self-shielding of molecular gas from foreground interstellar radiation. This allowed the formation of GMCs where runaway collapse leads to star formation (SF). Dense, gravitationally bound, and collapsing gas is accreted onto collisionless sink particles that abstract the last stages of the SF process to a sub-grid model due to the limited resolution of even this higher resolution simulation.

At gas densities $\rho_c > 10^{-21} \text{ g cm}^{-3}$ ($n_{\text{H}} \gtrsim 600 \text{ cm}^{-3}$) the gas is tested to determine if it is bound and collapsing and if so a sink particle is created. Dense gas with $\rho > \rho_c$ that comes within an accretion radius of 2.5 pc will then be accreted by the sink particle if bound to it. Given these densities and sizes, the sink particles represent small stellar (sub)-clusters. At these scales SF is still fairly inefficient, so only 5% of the accreted gas mass is converted into stars. In this sense every sink particle consists of a stellar component and a gas

component. Each stellar component is modelled as a stellar population whose initial stellar masses are drawn from an input Kroupa (2001) IMF. The massive stars drawn are evolved based on a simple stellar evolution model Maeder (2009) and at the end of their life-time they produce a supernova (SN) feedback event, disrupting the clouds and closing the ISM life-cycle. Note that this approach is different from the traditional star particle approach of cosmological simulations as we explicitly consider the gravitational binding of the gas to model ISM fragmentation and then include subsequent gas accretion.

The gas component trapped within the sink particle is progressively ejected and re-added to the gas phase with every SN event. After the last SN of a particular sink, the sink particle includes only stellar mass and is converted to a different particle type that represents an old stellar population. By drawing randomly using Poisson sampling from the IMF, it could occur that in particular cases no massive star is generated within the sink. In that case, after a trial period of 10 Myr, the gas component is ejected from the sink without a SN event and the sink is then converted to an old stellar population particle. Significant approximations of the AREPO-M51 simulation include the lack of early stellar feedback such as winds, jets, and ionising radiation and the absence of magnetic fields.

4.3.2. Parametrizing the density PDF

The AREPO-M51 simulation contains star-bursting regions as well as regions with hardly any ongoing star formation. The question we pose is; how does the gas density PDF change from one region to another and can we parametrize it for use in SIMBA? To investigate this, we divide the AREPO-M51 simulation volume into cubes of 200 pc on a side and calculate the gas density PDF within each cube. The region size of 200 pc was chosen in order to represent typical SKIRT cell sizes, and at the same time be large enough to contain enough elements in AREPO-M51 to properly sample the gas density PDF. We expect the PDF to move towards higher densities as the volume-averaged gas density of a region increases, but also as SFR density increases (Kainulainen et al. 2009). Figure 14 in Appendix D shows the resulting mean PDFs of cells within 200 pc regions using teal dashed lines. In grey we show the 1σ spread for 12 bins of volume-averaged density, $\langle n_H \rangle_V$, and SFR density, $\langle n_{\text{SFR}} \rangle_V$. A red vertical dashed line in each panel indicates the critical density, above which the cell data starts to be incomplete as some gas cells are converted into sink particles.

Due to the spread in PDFs, as indicated with grey areas in Figure 14, we cannot just interpolate between PDFs. Instead, we make a parametric fit, such that the fit parameters depend on $\langle n_H \rangle_V$ and $\langle n_{\text{SFR}} \rangle_V$. For the parametric fit, we build on previous work showing that the density distribution of a collapsing cloud can be approximated by a log-normal with a power-law tail. Simulations of gravo-magneto-hydrodynamic turbulent fragmentation have shown that the density field of an isothermal star-forming cloud is well approximated by a log-normal distribution at low density and a power-law distribution at high density (Klessen 2000; Collins et al. 2012; Burkhardt et al. 2015; Mocz et al. 2017; Padoan et al. 2017; Burkhardt 2018):

$$p_{LN+PL}(s) = \begin{cases} N \frac{1}{\sqrt{2\pi}\sigma_s} e^{-\frac{(s-s_0)^2}{2\sigma_s^2}}, & s < s_t \\ N e^{-\alpha s}, & s > s_t, \end{cases} \quad (1)$$

where N is the normalization constant, s_0 is the mean logarithmic overdensity, and s is the logarithmic overdensity:

$$s \equiv \ln(\rho/\rho_0) \quad (2)$$

where ρ_0 is volume-averaged density of the entire cloud. The transition density, s_t , above which the distribution approximates a power-law, was shown by Burkhardt (2018) to relate to the log-normal width, σ_s , and power-law slope, α , as:

$$s_t = (\alpha - 1/2)\sigma_s^2 \quad (3)$$

In Figure 14 in Appendix D, a fit is made to all mean PDFs by combining a log-normal function with a power-law at the high-density end, keeping σ_s and α as free parameters. However, this fit does not take into account gas mass locked in sink particles. The gas in sink particles where no SN has exploded will be dense and distributed in relatively undisturbed GMCs, while gas in other sink particles with supernova remnants (SNR) has already been at least partly dispersed in the surrounding ISM due to SN feedback. In order to account for the dense gas mass in sink particles, we divide the sink particles in two categories:

- Category I sink particles have stellar populations that produce no SN explosions. Here, we expect the gas to be relatively undisturbed and we count all gas mass in the particle as dense gas following a power-law density PDF regardless of the sink particle age. The percentage of sink particles in this category is only 0.13%.
- Category II sink particles have formed or will produce at least one SN. Due to feedback from

the SN explosion, a GMC will not survive for long in this environment. In a study looking for OH(1720 MHz) masers in the inner Galaxy, [He-witt & Yusef-Zadeh \(2009\)](#) found that dense gas can survive accompanying 15% of SNRs. Considering that SNRs are visible only during the first ~ 0.1 Myr of their lifetime and assuming that SNe occur at a roughly constant rate after the first SNe go off, we can convert the SNR number fraction of 15% into an upper age limit; We count gas in sink particles with SNRs as being dense gas, if the sink particle age since the first SN exploded is less than 15% of the longest SNR lifetime. The first SNe, created by the most massive stars, are expected to begin exploding at a sink particle age of $10^{6.5}$ yr or ~ 3 Myr (e.g. [Yungelson et al. 2008](#)). The percentage of sink particles in this category is 22.7%.

For the remaining sink particles, we do not count their internal gas mass as dense, but rather as gas that will be re-dispersed by feedback. [Figure 5](#) illustrates the selection criteria and the distribution in sink particle ages and gas masses. A main branch can be seen of sink particles that start out with a mass of $\sim 2 \times 10^5 M_\odot$ and begin to reduce in gas mass after a period of roughly $10^{6.5}$ yr when SNe start to disperse the gas. The sharp cutoff in initial gas mass at $2 \times 10^5 M_\odot$ is a result of retaining nominal resolution in the collisionless particles by allowing new sink particles to form instead of having single particles with anomalously high mass. Another fraction of sink particles starts out with much lower masses and some particles never accrete enough mass to form a massive star and produce a SN (teal circles).

The additional sink gas mass is expected to change only the high density portion of each PDF, as it has already passed the density threshold of $\rho_c = 600 \text{ cm}^{-3}$. We first attempt to accommodate the sink gas mass by iterating on the power-law slope until enough additional mass has been added. This method results in the orange dashed curves in [Figure 12](#) in [Appendix D](#), while the orange solid curves are combined log-normal and power-law fits made to the new distributions. This method works in all but the most dense and star-forming cells (bottom right panel in the same figure), where the sink gas mass fraction of 93% results in a nonphysical positive power-law slope. In the latter case we fix α to -1.5 as expected for evolved clouds undergoing rapid gravitational collapse ([Girichidis et al. 2014](#)) while allowing the width, σ_s , to change, moving the center such that the new log-normal matches the slope of the original log-normal on the low-density side.

The resulting fits, shown with orange curves in [Figure 14](#), are used as look-up tables for each cell in the

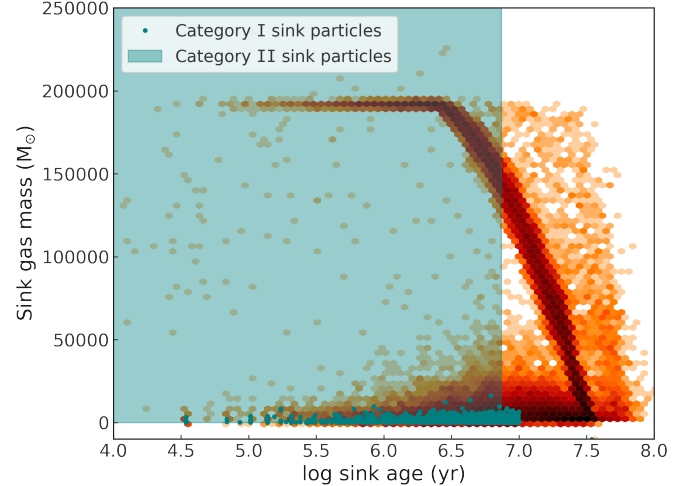


Figure 5. Distribution of sink particle gas mass and age. The teal circles and teal shaded area illustrate the selection criteria of category I and II sink particles, respectively, as described in [Section 4.3](#).

SKIRT output, by interpolating in $\langle n_H \rangle_V$ and $\langle n_{\text{SFR}} \rangle_V$. For cell densities below the minimum grid point in the AREPO-M51 look-up tables, we adopt a single, narrow log-normal PDF corresponding to a Mach number of 1 and a turbulent forcing parameter $b = 1/3$ ([Federrath et al. 2008](#)) without the power-law tail. All PDFs are cropped to the density range from $n_H = 10^{-4} \text{ cm}^{-3}$ to $n_H = 10^7 \text{ cm}^{-3}$.

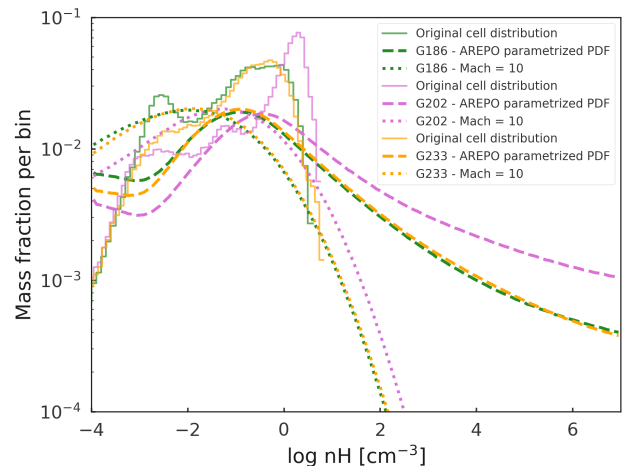


Figure 6. Examples of density PDFs for the same three SIMBA-25 galaxies as shown in [Figure 3](#), here shown with different colors.

Examples of the resulting galaxy-wide density PDFs can be seen in [Figure 6](#) for the same galaxies as shown in [Figure 3](#). The original density PDF in the cell data

Table 2. Parameters for the one-zone CLOUDY models.

Model parameter	Min value	Max value	step size
$\log n_{\text{H}} [\text{cm}^{-3}]$	-4	7	1
$\log Z [Z_{\odot}]$	-2	0.5	0.5
$\log N_{\text{H}} [\text{cm}^{-2}]$	17	22	0.5
$\log F_{\text{FUV}} [G_0]$	-7	4	1
log DTM ratio	-2	-0.2	0.2

from SKIRT (solid line) is compared to the derived PDF adopting a single log-normal with Mach number 10 and forcing parameter $b = 1/3$ versus the approach described above in dotted and dashed lines, respectively.

4.4. FIR line emission with CLOUDY (step 4)

The final step of SÍGAME v3 is to derive the line emission, having gathered all the necessary information by post-processing the simulation. To this end, we use a library of one-zone CLOUDY models that span the parameter ranges listed in Table 2. For each value of the F_{FUV} flux, the cosmic ray ionization rate ξ is scaled as

$$\xi = (F_{\text{FUV}}/G_0)\xi_0, \quad (4)$$

where $\xi_0 = 10^{-16} \text{ s}^{-1}$ is taken as the average Milky Way value (Indriolo et al. 2007) and the Solar neighborhood FUV flux $G_0 = 1.6 \times 10^{-3} \text{ erg cm}^{-2} \text{ s}^{-1}$ (Habing 1968).

The one-zone CLOUDY models must now be sampled according to the gas density PDFs found in Section 4.3, such that each combination of $\langle n_{\text{SFR}} \rangle_V$ and $\langle n_{\text{H}} \rangle_V$ in the galaxy simulations corresponds to a density PDF-weighted sum of the 12 different one-zone CLOUDY models along the $\log n_{\text{H}}$ axis that correspond to that region’s other parameters ($\log Z$, $\log N_{\text{H}}$, $\log F_{\text{FUV}}$ and $\log \text{DTM}$). For this step, six grid points in $\langle n_{\text{H}} \rangle_V$ (from 10^{-4} to 10^2 cm^{-3}) and four grid points in $\langle n_{\text{SFR}} \rangle_V$ (from $10^{-2.5}$ to $10^{0.5} \text{ M}_{\odot} \text{ yr}^{-1}$) are used. For each combination of $\langle n_{\text{H}} \rangle_V$, $\langle n_{\text{SFR}} \rangle_V$ we take the gas density PDF that comes closest in terms of both values, and shift the center of the lognormal to exactly match $\langle n_{\text{H}} \rangle_V$. This shift is performed to ensure that the PDFs generated are not only centered on the six chosen $\langle n_{\text{H}} \rangle_V$ grid points, but can fill out the density space and generate a smooth total PDF as shown in Fig. 6. The sampling of one-zone CLOUDY models is carried out for all combinations of N_{H} , F_{FUV} , Z , and DTM ratio, leading to a look-up table of 190,080 different combinations of one-zone CLOUDY models, with one such table for each spectral line considered.

4.4.1. User-defined sub-grid attenuation function

The SKIRT calculation yields the average interstellar radiation field in cells with sizes ranging from 19 pc to 6.3 kpc (for the SIMBA-100 galaxies), but due to the resolution limit of the underlying SIMBA simulation, additional attenuation by parsec-size sub-structures is not taken into account by SKIRT. As a way of compensating for this lack of resolution, we have included in the framework an optional user-defined function to add extinction on sub-grid scales. In practice, this is done by generating a one-zone CLOUDY grid as described in Section 4.4 but for which the incident spectra were attenuated using the “extinguish” command in CLOUDY. This command diminishes the incident spectrum with a simple power-law corresponding to an intervening slab of gas of fixed column density, which is set to 10^{24} cm^{-2} here. For the SIMBA simulations at hand, we test the framework with a very simple extinction function, that only adds extinction to CLOUDY grid cells of density above 10^2 cm^{-3} . When constructing the look-up table by sampling the gas density PDFs (Section 4.3), these extinguished models were sampled for densities $n_{\text{H}} > 10^2 \text{ cm}^{-3}$ (ξ was not modified for these models). This procedure roughly mimics a scenario in which high density gas regions are the most shielded from ionizing photons. For a different base simulation, the attenuation function might need to be revised or completely omitted in the very high resolution case. In the following section we will compare the results with and without this additional function.

5. VALIDATION OF THE CODE

The measure by which we evaluate the success of a given sub-grid model is how well it matches observed FIR emission line luminosities of galaxies. In this paper, we restrict the comparison to nearby galaxies observed with *Herschel* or the *Infrared Space Observatory* as found in the literature.

5.1. Simulation runs

In order to compare different assumptions in the sub-grid process, we perform four different runs on the same $z \sim 0$ sample from the SIMBA-100 box as well as one run on galaxies selected in the SIMBA-25 box. The names of the different runs are listed in Table 3. In the first run (100MPC_M10 in Table 3), we report the line luminosities that SÍGAME returns when the density fragmentation is carried out the “traditional way” with a single log-normal density PDF corresponding to a Mach number 10 and a forcing parameter of $1/3$. Next, we applied SÍGAME v2 to the same set of galaxies, using the modifications to the code described in Leung et al. (2020) together with a new

Table 3. The different `síGAME` runs compared in this study.

Run name	Description
100Mpc_M10	Adopting one log-normal with Mach number 10 with a forcing parameter 1/3 for the sub-grid density profile (cf. Section 4.3).
100Mpc_SíGAMEv2	Comparison run with <code>síGAME</code> v2 applied to the <code>SIMBA-100</code> sample.
100Mpc_arepoPDF	Adopting density PDFs with a powerlaw tail as parametrized for a higher resolution <code>AREPO-M51</code> simulations (cf. Section 4.3). This is our “default run”.
25Mpc_arepoPDF	Same as “arepoPDF” but for the <code>SIMBA-25</code> simulation volume (cf. Section 3).
100Mpc_arepoPDF_no_ext	Same as “arepoPDF” but without the additional extinction function described in Section 4.4.1.

`CLOUDY` grid at $z = 0$ (`100MPC_SíGAMEv2`). The next simulation run adopts the new gas fragmentation scheme described in this paper, and will be deferred to as our “default run” (`100MPC_AREPOPDF`). The default settings are also applied to a smaller sample of 240 galaxies in the `SIMBA-25` box as a convergence test (`25MPC_AREPOPDF`). Finally, we also investigate the resulting line emission when not including the additional sub-grid attenuation function as described in Section 4.4.1 and otherwise adopted in the default run (`100MPC_AREPOPDF_NO_EXT`).

5.2. Observations used

In the comparison with observations, we include all galaxies found with total line luminosities and SFR estimates. This is a rough validation check, since both observed and simulated galaxies span a wide range of galaxy types, but even so serves to show whether the model can at all reproduce the observed range in values.

Almost all of the FIR emission lines considered here have been tested as tracers of SFR with varying degrees of success. As a result, the literature holds a vast number of nearby galaxies with both infrared emission line measurements and derived SFRs. In order to best compare with observations, we estimate the SFR of the model galaxies as a mean over the past 100 Myr, and not the instantaneous SFR of gas particles. Fur-

thermore, all SFRs derived using a [Salpeter \(1955\)](#) IMF have been converted to the equivalent SFR of a [Chabrier \(2003\)](#) IMF as in the `SIMBA` simulation, by adopting a -0.24 dex correction (e.g. [Mitchell et al. 2013](#)). The observed SFRs were obtained with various methods summarized here; For the sample of mixed type galaxies in [Kamenetzky et al. \(2016\)](#) and the LIRGS in [Díaz-Santos et al. \(2013\)](#), the far-infrared luminosities, L_{FIR} ($40\text{--}120\ \mu\text{m}$ and $42.5\text{--}122.5\ \mu\text{m}$ in the two respective cases), of those papers are converted into SFRs according to [Kennicutt \(1998\)](#). For the sample of dwarf galaxies of [Cormier et al. \(2015\)](#), SFRs come from [Rémy-Ruyer et al. \(2015\)](#) who derived SFR from FUV and $\text{H}\alpha$ luminosities, corrected for dust attenuation. The galaxy sample of [Schruba et al. \(2012\)](#) contains CO(2-1) luminosities for 16 dwarf galaxies (with one galaxy in common with the [Cormier et al. \(2015\)](#) sample) as well as CO(1-0) luminosities for nearby galaxies compiled from the literature, of which we show 22 CO(1-0) observations from the HERA CO-Line Extragalactic Survey (HERACLES; [Leroy et al. 2009](#)) and 20 from [Calzetti et al. \(2010\)](#). For the 16 dwarf galaxies, SFRs in [Schruba et al. \(2012\)](#) were calculated as a combination of FUV and $24\ \mu\text{m}$ emission following the approach in [Bigiel et al. \(2008\)](#) and [Leroy et al. \(2008\)](#). For the SFRs of the 50 nearby galaxies we use the values compiled from literature in [Schruba et al. \(2012\)](#), and refer to the references therein for specific methods. Finally, for the sample of main sequence and starburst galaxies of [Brauer et al. \(2008\)](#), we convert the reported $63\ \mu\text{m}$ flux to an SFR using the $70\ \mu\text{m}$ monochromatic SFR conversion relation of [Calzetti et al. \(2010\)](#).

5.3. Line luminosity vs. SFR correlations

Figure 7 shows line luminosities as a function of SFR for all 8 emission lines listed in Table 1 with default settings and the `SIMBA-100` galaxy sample `100MPC_AREPOPDF` (see Table 3). Galaxy symbols are color-coded by their molecular gas mass surface density, calculated using the amount of H_2 predicted by `CLOUDY` within the gas half-mass radius from `CAESAR`. The panels are organized such that the left column contains line emission tracing primarily PDRs and ionized regions of the ISM, while the right shows tracers of primarily neutral and molecular regions in the ISM. In all panels, a black dashed line indicates a log-linear fit to the observed line luminosities binned in terms of SFR. For panels with $[\text{C II}]$, $[\text{O III}]\lambda 88$, and $[\text{O I}]\lambda 63$ line emission, the relations from [De Looze et al. \(2014\)](#) for local starburst and dwarf galaxies are also shown.

For all emission lines except the $[\text{N II}]$ and $[\text{O I}]\lambda 63$ lines, there is a good overall agreement with observa-

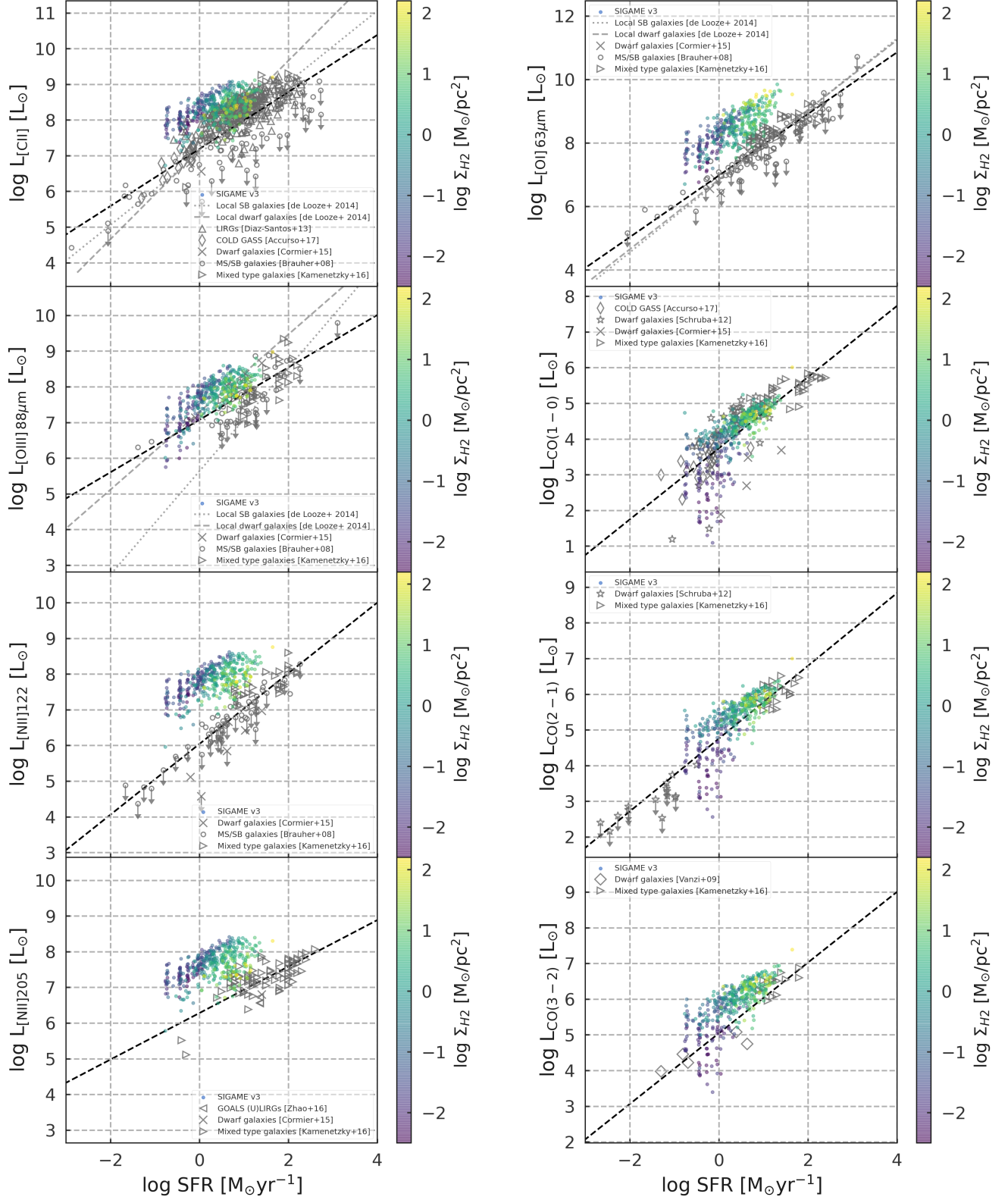


Figure 7. Correlations between line emission and SFR for the *SIGAME* results compared to observations of nearby galaxies: LIRGs (Díaz-Santos et al. 2017), dwarf galaxies (Madden et al. 2013; Cormier et al. 2015), main-sequence and starburst galaxies (Brauer et al. 2008), (U)LIRGs (Farrah et al. 2013; Zhao et al. 2016), the randomly selected $0.01 < z < 0.02$ COLD GASS galaxy sample of Accurso et al. (2017), and the mixed sample of Kamenetzky et al. (2016) and Schrubba et al. (2012). For the dwarf galaxy sample, we only include seven galaxies with galaxy-integrated luminosities, following the criteria of Accurso et al. (2017). For the sample of Kamenetzky et al. (2016), we include only galaxies with optical sizes smaller than $47''$ as a very conservative measure to insure that the *Herschel*/PACS field of view included all line emission. See the text for how SFR was calculated.

tions. The simulated line luminosities span the range in observed line luminosities for the same range in SFRs. The largest discrepancy between observations and simulations can be found for the [N II] and [O I]63 lines, originating in primarily H II regions and dense, neutral gas, respectively (Table 1). Here, the median deviation of our models above the log-linear fit to all observed samples, is 1.6, 1.2 and 1.2 dex for [N II]122, [N II]205 and [O I]63, respectively. Both [NII] lines are excited by collisions with electrons, with [N II]122 having a higher critical density than [N II]205 (Table 1). The slightly higher offset for [N II]122 compared to [N II]205, translates into a higher [N II]122/205 line ratio than observed, indicating that our simulated galaxies have on average higher electron densities, since this line ratio is expected to increase with electron density (e.g. Herrera-Camus et al. 2016). [O I]63 on the other hand arises in PDRs of much higher densities, and rather than depending on density, the excitation of [O I]63 depends on the temperature of the gas as set by the FUV radiation that heats the gas primarily through the photoelectric effect. In the current SÍGAME framework, the local FUV flux is derived with SKIRT radiative transfer together with an optional additional attenuation as described in Sections B and 4.4.1, respectively. Without the last step of additional attenuation, we see an even larger median deviation of 2.0 dex as will be further discussed in Section 6, confirming that the radiation field strength and amount of attenuation is indeed an important factor in setting the [O I]63 luminosity.

In all cases of CO line emission, a large fraction of our simulated galaxies with $\text{SFR} \lesssim 1 M_{\odot}/\text{yr}$ display a reduced CO luminosity, forming a small "tail" of low luminosity galaxies reaching down below the observed relation by ~ 1 dex. Galaxies in this tail have very low molecular surface densities ($\lesssim 1 M_{\odot} \text{pc}^{-2}$) and low metallicities ($\langle Z \rangle_{\text{SFR}} \lesssim 0.5 Z_{\odot}$). In the panel with $L_{\text{CO}(1-0)}$, we see that this is in agreement with the mixed and dwarf galaxy sample of Schrubba et al. (2012) in CO(2-1) and CO(2-1), respectively (stars). This agreement is presumably due to the overall low metallicity of the dwarf sample, extending down to $\sim 0.03 Z_{\odot}$ (M81 Dw A; Schrubba et al. 2012), although our galaxy sample only goes down to $0.1 Z_{\odot}$ in SFR-weighted metallicity. While the observed galaxies would seem to agree with our simulations in terms of CO luminosity, it is worth pointing out that these galaxies have much lower [C II] luminosities than our simulated galaxies as shown in Figure 8 which shows CO(1-0) against [C II] luminosity for the 100MPC_AREPOPDF, 100MPC_AREPOPDF_NO_EXT and 25MPC_AREPOPDF runs. The galaxy samples of Kamenetzky et al. (2016),

Cormier et al. (2015), and Accurso et al. (2017) are also shown with the latter two sample galaxies color-coded by metallicity for comparison with the simulated galaxies. To guide the eye, a log-linear fit is made to the observations and shown in dashed black line. As dictated by the brown contour lines, the omission of additional attenuation at high densities results in larger deviations from the observed [C II]-CO relation.

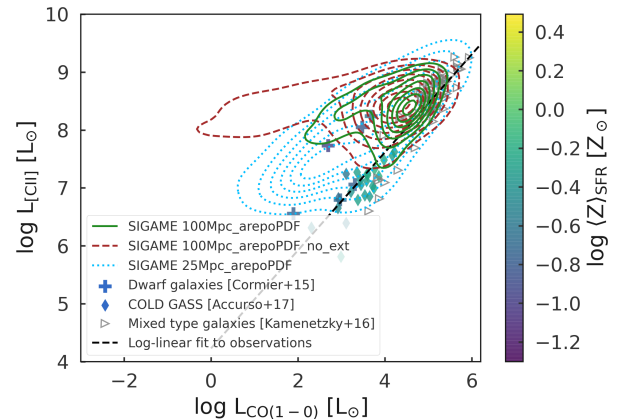


Figure 8. [C II] versus CO(1-0) luminosity for the SÍGAME v3 results (100MPC_AREPOPDF run; green contours, 100MPC_AREPOPDF_NO_EXT run; brown dashed contours and 25MPC_AREPOPDF run; blue dotted contours) compared to the observed galaxy samples of Kamenetzky et al. (2016), Cormier et al. (2015) and Accurso et al. (2017). The simulated galaxies and (where possible) the observed galaxies have been color-coded by metallicity. The dashed line indicates a log-linear fit to the observations alone.

5.4. Comparison of different SÍGAME runs

Figure 9 condenses the data in Figure 7 into median deviations between the simulated galaxy line luminosities and a linear fit to the observed ones (black dashed lines in Fig. 7) as a function of SFR. The standard deviation of the offsets for the observed galaxies is indicated with a dark grey envelope. The different SÍGAME runs listed in Table 3 can now be compared for each of the eight emission lines considered here, with the fine-structure lines sorted in order of increasing critical density (Table 1).

For run 100MPC_M10, the resulting deviations from observations are shown with orange bars. Surprisingly, this simple assumption does a very good job for the ionized species of [N II]122, [N II]205, [O III]88 and [C II], but completely underestimates CO emission and to a lesser degree [O I]63 as well. The [O I]63, CO(1-0), (2-1) and (3-2) lines fall below the observed line-SFR relation by median deviations of 0.6, 3.1, 4.1 and 4.1 dex,

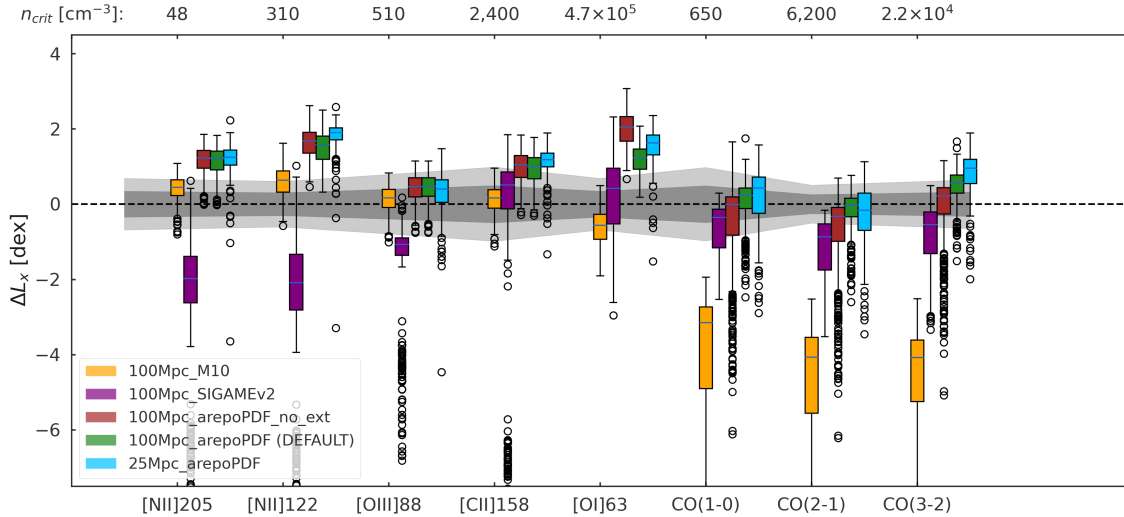


Figure 9. Box plot performance comparison of the different `SIGAME` runs listed in Table 3 for all lines considered here, with the fine-structure lines sorted in order of increasing critical density. Light and dark grey shaded areas represent 1 and 3 σ spread in the observations. The boxes extend from the lower to the upper quartile values, whiskers to a factor 1.5 wider range, and open circles indicate outliers outside the whiskers. The critical densities are from Table 1 with ρ_{crit} of atomic hydrogen for [C II].

respectively. The underestimation of the molecular lines is not surprising, given that the density PDF does not extend significantly beyond densities $> 10^2 \text{ cm}^{-3}$ where molecules form (see Fig. 6).

With run `100MPC_SIGAMEv2` (purple bars), we test how well the previous `SIGAME` framework, which has so far only been applied at $z \sim 2$ and above, works for the `SIMBA-100` $z = 0$ sample. While this version of the code gives good results for [C II] and [O I]63, and comes closer to the observed CO luminosities than the `100MPC_M10` run, it significantly underestimates the [N II] lines. For all lines except [O I]63, this version also produces outliers with extremely low line luminosities, as shown with open circles (and indeed, the plot does not extend to show all outliers).

The test run without additional extinction, `100MPC_AREPOPDF_NO_EXT` (brown bars), displays a better agreement with the observed CO and [O III]88 luminosities than the `100MPC_M10` run, but our PDF framework fares worse for all other lines. In particular the [O I]63 line predictions fall above the observed luminosities by a median deviation of 2.0 dex, and there are still some very low CO luminosity predictions.

The default run of the current version of `SIGAME`, `100MPC_AREPOPDF` (green bars) comes closest to all line luminosities simultaneously, with the least number of outliers. The [N II]122 and [O I]63 line predictions show the poorest match with observations, remaining overestimated by median deviations of 1.6 and 1.2 dex, respectively. Compared to the run without additional

attenuation, the [O I]63 line over-predictions are reduced by about 1 dex from 2.0 dex to 1.2 dex above the observational [O I]63–SFR relation, and the tail of low CO luminosities is reduced in length by several dex. The continued overestimation of the [O I]63 and [N II] line emission, however, suggests that a more careful treatment of the sub-grid attenuation and/or other features remains missing. A proper treatment of the flux distribution on these scales would require considerations about the properties of natal clouds around young stars as demonstrated with the one-dimensional stellar feedback model `WARPFIELD` (Rahner et al. 2017). [C II] and [O III]88 remain slightly overestimated, both of which originate mainly in the atomic ISM phase in our model, hinting at an overestimation of atomic gas mass vs ionized gas mass in our gas fragmentation scheme. We do not consider the overestimation of CO(3-2) a problem due to the lack of observations compiled here and the possibility that the relation with SFR is not linear as the large deviations suggest.

Finally, the test run with default settings at higher mass resolution, `25MPC_AREPOPDF` (blue bars), shows deviations consistent with the `SIMBA-100` sample, indicating that the `SIGAME` results converge well with increasing mass resolution. In Fig. 15 in Appendix E we investigate in more depth how well the two simulation runs agree with one another for a range of physical galaxy properties, finding that for similar galaxies, the luminosities are within 1 dex of each other with slightly higher deviations towards low values of M_* , M_{gas} , SFR

and $\langle Z \rangle_{\text{SFR}}$ where the gas particle number in SIMBA-100 drops below 500.

5.5. Moment 0 maps of line emission

Fig 10 shows moment0 maps of CO(1-0), [C II] and [O III]88 emission constructed for the same galaxies from SIMBA-100 shown in Figure 3. The output datacube from SÍGAME contains spatial information, cell sizes and cell luminosities that were combined to derive the surface brightness of each pixel in the final image, weighing each cell by its volume filling factor within the column covered by each pixel². We note that the calculation of the moment0 maps assumes an ISM fully transparent to the FIR line emission, an assumption that might not hold for shorter wavelengths. Some expected differences in how the emission lines trace the ISM can be observed, such as the preference for [C II] to arrive from PDRs near star forming regions compared to the broader CO(1-0) emission, and the relatively concentrated [O III]88 emission restricted to H II regions experiencing harder radiation fields from young stars.

6. DISCUSSION

6.1. Comparison with previous models

We can compare our [C II]-SFR relation with that found through similar techniques and hence better understand the decisive differences between the models. Figure 11 shows the [C II]-SFR relations found by SÍGAME for the SIMBA-100 galaxies with the 100MPC_AREPOPDF and run (green contour lines) together with the relations derived by Popping et al. (2019) and Ramos Padilla et al. (2020). From the 100MPC_AREPOPDF run, we also show the distribution of only MS galaxies, chosen to be within the 16 and 84 percentile of the Salim et al. (2018) relation (purple dashed contour lines). The distribution of SÍGAME simulated galaxies are generally too high compared with observations and exhibits a much shallower slope towards lower SFRs, where our model seems to overpredict the [C II] luminosities by about 1 dex. When selecting only MS galaxies, the agreement with observations improves only at the high SFR-end of $\gtrsim 1 M_{\odot} \text{ yr}^{-1}$.

6.2. Choice of simulation for the fragmentation task

We have only shown results for the present framework using one type of simulation, namely the AREPO suite of M51 realizations. We also examined an AREPO simulation of the central molecular zone (Sormani et al. 2020), but found no significant change from the PDFs extracted

and shown in Figure 14. However, choosing a completely different galaxy simulation technique (e.g. models run with adaptive mesh refinement codes such as RAMSES, ENZO, or ATHENA Teyssier 2002; Bryan et al. 2014; Kim & Ostriker 2017) might return different PDFs, the effect of which we have not studied. Instead, we have focused on making the current version of SÍGAME flexible and publicly available so that the user can include any high resolution simulation for the gas fragmentation if they so desire.

6.3. Small-scale radiation field structure

As discussed in the previous section, this version of SÍGAME fragments the gas density on scales smaller than the SKIRT cell sizes (typically larger than ~ 15 pc), thereby allowing for clumps of higher densities on scales not resolved by the parent simulation. In a similar manner, we could also expect the radiation field to be fragmented such that the mass-weighted FUV flux distribution on parsec scales can differ substantially from the overall cell mean flux value and allow for parsec-size features such as H II regions or shielded, dense, molecular cores. Judging from the overall agreement between simulated and observed lines, we speculate that most of the FIR lines considered here arise from structures of larger extent where parsec resolution in radiation is not necessary, with the exception of [O I]63, which is heavily overestimated.

6.3.1. Missing treatment of active galactic nuclei

While the co-evolution of active galactic nuclei (AGN) and their host galaxies is simulated in SIMBA, the current version of SÍGAME does not include any effects of AGN presence, such as additional heating and radiation. The additional X-ray heating has been shown to increase excitation of high-J CO lines at high redshifts (Vallini et al. 2019).

6.3.2. Missing shock-heating of the gas

In starburst galaxies and mergers, shocks are expected to act as an additional heating source in the ISM. Although the next version of CLOUDY may include a treatment for shock-heated gas, the current version of CLOUDY iterates to find a thermal and ionization equilibrium, thereby ignoring any shocked state of the gas that might be present in the simulation. One way to treat shock-heated gas, would be to set up a separate grid of models, following the technique used for MAPPINGS III (Allen et al. 2008). Turbulence (2–10 km s^{-1} in velocity dispersion) and/or density-dependent magnetic fields are also believed to play a role in setting the [O I]63 emission, through their effect on line width, shielding and pumping, chemical and thermal state of

² https://github.com/jaymotka/moment0_maps

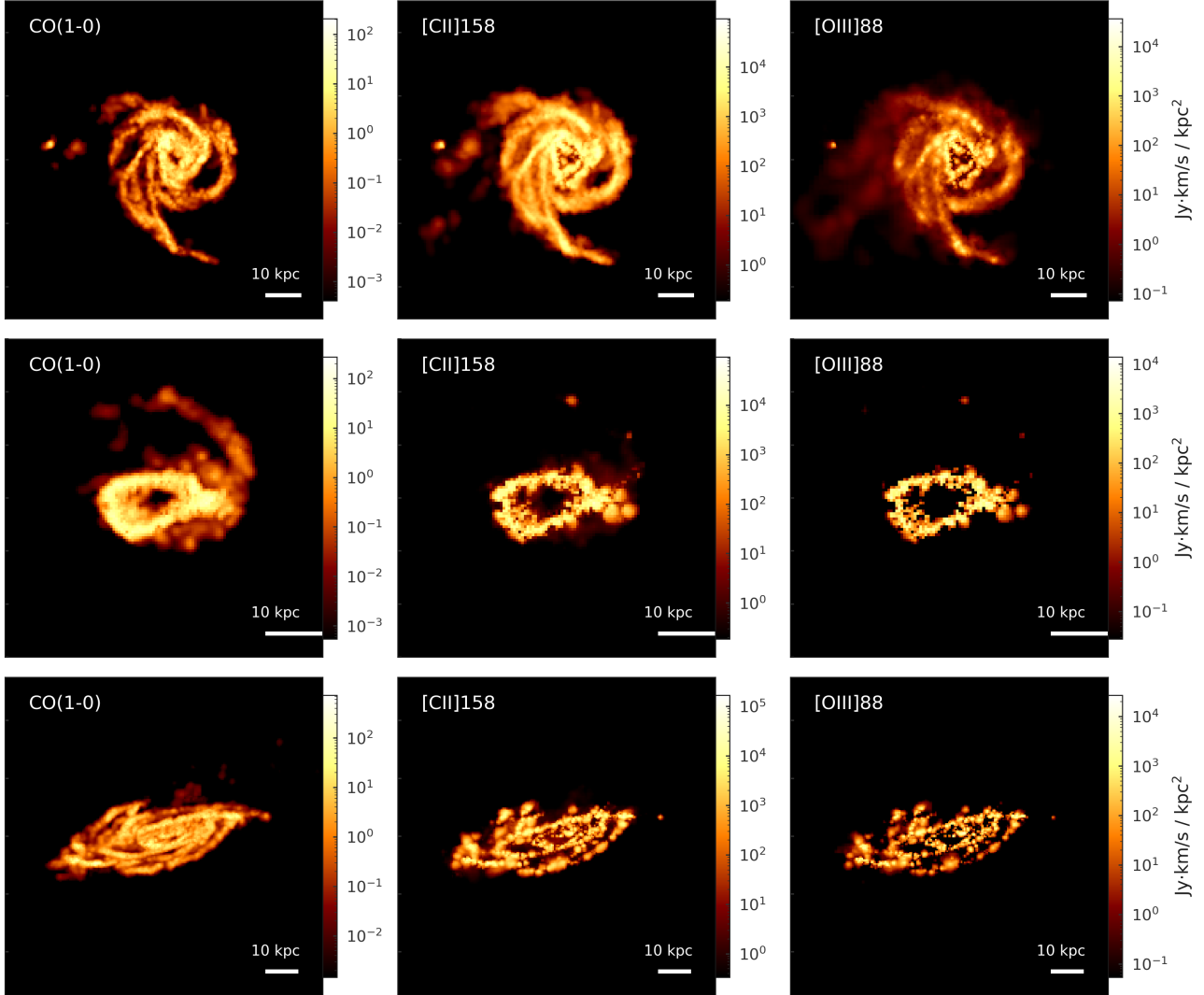


Figure 10. Moment0 maps of the same galaxies shown in Fig 3, for three of the emission lines investigated here.

the gas (Canning et al. 2016). However, testing the effect of these would require CLOUDY models of more than one zone where optical depth is taken into account.

7. CONCLUSIONS

This paper introduces an improved algorithm for estimating FIR line emission from large-volume cosmological galaxy simulations using coarse numerical resolution. We post-process such simulations using a sub-grid model that estimates the distribution of dense gas up to densities of $\sim 10^7 \text{ cm}^{-3}$. This fragmentation scheme results in gas at lower densities being compressed to higher densities, and hence affects emission lines tracing all ISM phases. We test the scheme on eight low-to-medium density ISM tracers.

The density distribution on sub-grid scales is modeled by sorting and parametrizing resolved regions in

higher-resolution simulations and interpolating on the parametrized functions to set the density distribution for the cosmological simulations. This statistical approach avoids any assumption about the size and shape of molecular clouds, the turbulence within those clouds, or the existence of pressure equilibrium between the dense and more diffuse ISM phases. As a demonstration of this scheme, we use data with sub-parsec resolution from a model of M51 with AREPO (Tress et al. 2020). Density PDFs are sampled in 200 pc regions and binned in terms of the volume-averaged hydrogen and SFR density of each region. The resulting mean PDFs are parametrized and used to generate PDFs by interpolation for each resolution element of the cosmological simulation to generate gas densities $\sim 10^2\text{--}10^6 \text{ cm}^{-3}$ otherwise not present in the cosmological simulation re-

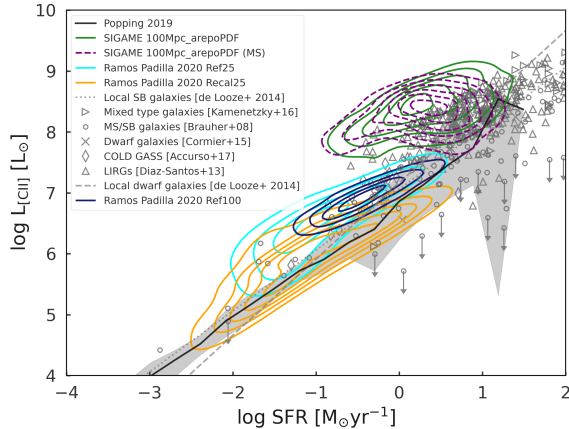


Figure 11. Comparison of `SIGAME v3` [C II]-SFR relation (100MPC_AREPOPDF; green, MS-only galaxies: purple dashed contour lines) with other recent modeling efforts: a multi-phase model of the ISM used as a post-processing step for the EAGLE cosmological hydrodynamical simulations (cyan, orange, and dark blue contour lines; Ramos Padilla et al. 2020), and the $z = 0$ [C II]-SFR relation found by Popping et al. (2019) using SAMs (black line), with a $1-\sigma$ shaded region. Observations of local dwarf and starburst galaxies by De Looze et al. (2014) are shown as grey symbols for comparison with the models.

sults. As a future extension, this approach could also be used to develop a new SFR prescription for cosmological simulations.

The local radiation field strength is determined with the radiative transfer code SKIRT, which calculates the local dust-attenuated stellar spectrum. The SWIFT-SIMIO package is used to map gas properties from the cosmological simulation output to the cell structure from SKIRT. Additional attenuation by gas is implemented through a set of CLOUDY models, by matching the transmitted spectrum in the NIR-to-FUV of a certain column density of gas to the dust-attenuated spectrum of SKIRT for each gas cell. Line emission and chemical information are derived from an extensive grid of 95,040 CLOUDY 1-zone models, sampled according to the local density PDF to create a library totalling 190,080 models of different combinations of n_{H} , $\langle n_{\text{SFR}} \rangle_V$, N_{H} , F_{FUV} , Z and DTM ratio. Finally, to compensate for lack of resolution in the cosmological simulations used here, we add attenuation on sub-grid scales with a simple function that can be modified by the user to work on other simulation types. In this case, we add attenuation for CLOUDY grid models with $n_{\text{H}} > 10^2 \text{ cm}^{-3}$.

As validation of the method, results are compared to observed relations between line luminosity and SFR for a diverse sample of nearby galaxies and eight different

emission lines. The method is also checked against the default option of adopting a log-normal density profile drawn from Mach 10 isothermal turbulence for the sub-grid density profile, although we expect this method to fare poorly in the case of cosmological simulations. The validation leaves us with the following conclusions:

- The standard method in the literature of adopting the density PDF of Mach 10 isothermal turbulence for fragmenting gas on sub-grid scales results in FIR fine-structure line emission that agrees well with observations for lines originating mainly in the ionized ISM, but drastically underestimates lines from the neutral and molecular regions. For example, the CO(1-0), (2-1) and (3-2) rotational lines fall below the observed line-SFR relation by median deviations of 3.1, 4.1 and 4.1 dex, respectively.
- The novel method presented here of using a high resolution simulation and a new analytic PDF approach for the gas fragmentation results in emission lines that match observations well regardless of their origin in the ISM, with the noticeable exception of [N II]122, [N II]205 and [O I]63 that are overestimated by on average 1.6, 1.2, and 1.2 dex, respectively, compared to the observed line-SFR relation.
- We find that the resulting line emission of [O I]63 in particular is highly dependent on the user-defined attenuation function, without which the overestimation of the [O I]63 luminosities is about 1 dex higher still. This underlines the need for a more careful treatment of the radiation on sub-grid scales ($< 200 \text{ pc}$), where denser regions should produce additional attenuation of the interstellar radiation field than what is included in this framework by default.

We have presented `SIGAME v3` which is a flexible framework that can be adapted to any cosmological or galaxy simulation, and now with the option to further fragment the gas on sub-grid scales using a high-resolution simulation of choice. This tool may be useful for the interpretation of current data from e.g. ALMA, NOEMA and SOFIA as well as from future space and balloon missions such as JWST, GUSTO and ASTHROS.

ACKNOWLEDGMENTS

The authors thank Dr. Peter Camps for extensive support on SKIRT, Robert Thompson for developing CAESAR, and the YT team for development and support of YT (Turk et al. 2011). The authors are also grateful to the entire SIMBA collaboration that helped in the analysis and understanding of the SIMBA output. We acknowledge use of the PYTHON programming language version 3.7, available at <http://www.python.org>, Astropy (Astropy Collaboration et al. 2013; Price-Whelan et al. 2018), Matplotlib (Hunter 2007), NumPy (Harris et al. 2020), pandas (Wes McKinney 2010), SciPy (Virtanen et al. 2020) and SWIFTSIMIO (Borrow & Borrisov 2020). This research has made use of the NASA/IPAC Extragalactic Database (NED), which is funded by the National Aeronautics and Space Administration and operated by the California Institute of Technology. KPO is funded by NASA under award No 80NSSC19K1651. BB is partly funded by the Packard Fellowship for Science and Engineering. JB is supported by STFC studentship ST/R504725/1. RJS acknowledges an STFC ERF fellowship (grant ST/N00485X/1) and HPC from the DiRAC facility (ST/P002293/1). M-MML was partly funded by NSF grant AST18-15461. RT was supported by DFG SFB 881 “The Milky Way System” and the Excellence Cluster STRUCTURES (EXC 2181-390900948), as well as ERC Synergy Grant ECOGAL (project ID 855130). The Cosmic Dawn Center of Excellence is funded by the Danish National Research Foundation under grant No. 140.

Software: PYTHON version 3.7 (available at <http://www.python.org>), Astropy (Astropy Collaboration et al. 2013; Price-Whelan et al. 2018), AREPO (Springel 2010), CLOUDY version 17.2 (Ferland et al. 2017), SKIRT version 9.0 (Camps & Baes 2020), SWIFTSIMIO (<https://github.com/SWIFTSIM/swiftsimio>; Borrow & Borrisov 2020))

REFERENCES

- Accurso, G., Saintonge, A., Catinella, B., et al. 2017, *MNRAS*, 470, 4750, doi: [10.1093/mnras/stx1556](https://doi.org/10.1093/mnras/stx1556)
- Allen, M. G., Groves, B. A., Dopita, M. A., Sutherland, R. S., & Kewley, L. J. 2008, *ApJS*, 178, 20, doi: [10.1086/589652](https://doi.org/10.1086/589652)
- Alves, F. O., Cleeves, L. I., Girart, J. M., et al. 2020, *ApJL*, 904, L6, doi: [10.3847/2041-8213/abc550](https://doi.org/10.3847/2041-8213/abc550)
- Alves, J., Lombardi, M., & Lada, C. J. 2017, *A&A*, 606, L2, doi: [10.1051/0004-6361/201731436](https://doi.org/10.1051/0004-6361/201731436)
- Appleby, S., Davé, R., Kraljic, K., Anglés-Alcázar, D., & Narayanan, D. 2020, *MNRAS*, 494, 6053, doi: [10.1093/mnras/staa1169](https://doi.org/10.1093/mnras/staa1169)
- Astropy Collaboration, Robitaille, T. P., Tollerud, E. J., et al. 2013, *A&A*, 558, A33, doi: [10.1051/0004-6361/201322068](https://doi.org/10.1051/0004-6361/201322068)
- Bigiel, F., Leroy, A., Walter, F., et al. 2008, *AJ*, 136, 2846, doi: [10.1088/0004-6256/136/6/2846](https://doi.org/10.1088/0004-6256/136/6/2846)
- Borrow, J., & Borrisov, A. 2020, *The Journal of Open Source Software*, 5, 2430, doi: [10.21105/joss.02430](https://doi.org/10.21105/joss.02430)
- Brauher, J. R., Dale, D. A., & Helou, G. 2008, *ApJS*, 178, 280, doi: [10.1086/590249](https://doi.org/10.1086/590249)
- Bryan, G. L., Norman, M. L., O’Shea, B. W., et al. 2014, *ApJS*, 211, 19, doi: [10.1088/0067-0049/211/2/19](https://doi.org/10.1088/0067-0049/211/2/19)
- Burkhart, B. 2018, *ApJ*, 863, 118, doi: [10.3847/1538-4357/aad002](https://doi.org/10.3847/1538-4357/aad002)
- Burkhart, B., Collins, D. C., & Lazarian, A. 2015, *ApJ*, 808, 48, doi: [10.1088/0004-637X/808/1/48](https://doi.org/10.1088/0004-637X/808/1/48)
- Burkhart, B., & Mocz, P. 2019, *ApJ*, 879, 129, doi: [10.3847/1538-4357/ab25ed](https://doi.org/10.3847/1538-4357/ab25ed)
- Burkhart, B., Stalpes, K., & Collins, D. C. 2017, *ApJL*, 834, L1, doi: [10.3847/2041-8213/834/1/L1](https://doi.org/10.3847/2041-8213/834/1/L1)
- Calzetti, D., Wu, S. Y., Hong, S., et al. 2010, *ApJ*, 714, 1256, doi: [10.1088/0004-637X/714/2/1256](https://doi.org/10.1088/0004-637X/714/2/1256)
- Camps, P., & Baes, M. 2020, *Astronomy and Computing*, 31, 100381, doi: [10.1016/j.ascom.2020.100381](https://doi.org/10.1016/j.ascom.2020.100381)
- Canning, R. E. A., Ferland, G. J., Fabian, A. C., et al. 2016, *MNRAS*, 455, 3042, doi: [10.1093/mnras/stv2390](https://doi.org/10.1093/mnras/stv2390)
- Chabrier, G. 2003, *PASP*, 115, 763, doi: [10.1086/376392](https://doi.org/10.1086/376392)
- Chen, H. H.-H., Burkhart, B., Goodman, A., & Collins, D. C. 2018, *The Astrophysical Journal*, 859, 162, doi: [10.3847/1538-4357/aabaf6](https://doi.org/10.3847/1538-4357/aabaf6)
- Chevance, M., Kruijssen, J. M. D., Vazquez-Semadeni, E., et al. 2020, *SSRv*, 216, 50, doi: [10.1007/s11214-020-00674-x](https://doi.org/10.1007/s11214-020-00674-x)
- Collins, D. C., Kritsuk, A. G., Padoan, P., et al. 2012, *ApJ*, 750, 13, doi: [10.1088/0004-637X/750/1/13](https://doi.org/10.1088/0004-637X/750/1/13)
- Colombo, D., Hughes, A., Schinnerer, E., et al. 2014, *ApJ*, 784, 3, doi: [10.1088/0004-637X/784/1/3](https://doi.org/10.1088/0004-637X/784/1/3)
- Conroy, C., & Gunn, J. E. 2010, *ApJ*, 712, 833, doi: [10.1088/0004-637X/712/2/833](https://doi.org/10.1088/0004-637X/712/2/833)
- Conroy, C., Gunn, J. E., & White, M. 2009, *ApJ*, 699, 486, doi: [10.1088/0004-637X/699/1/486](https://doi.org/10.1088/0004-637X/699/1/486)
- Cormier, D., Madden, S. C., Lebouteiller, V., et al. 2015, *A&A*, 578, A53, doi: [10.1051/0004-6361/201425207](https://doi.org/10.1051/0004-6361/201425207)
- Cowie, L. L., & Songaila, A. 1986, *ARA&A*, 24, 499, doi: [10.1146/annurev.aa.24.090186.002435](https://doi.org/10.1146/annurev.aa.24.090186.002435)
- Davé, R., Anglés-Alcázar, D., Narayanan, D., et al. 2019, *MNRAS*, 486, 2827, doi: [10.1093/mnras/stz937](https://doi.org/10.1093/mnras/stz937)
- Davé, R., Thompson, R., & Hopkins, P. F. 2016, *MNRAS*, 462, 3265, doi: [10.1093/mnras/stw1862](https://doi.org/10.1093/mnras/stw1862)
- De Looze, I., Cormier, D., Lebouteiller, V., et al. 2014, *A&A*, 568, A62, doi: [10.1051/0004-6361/201322489](https://doi.org/10.1051/0004-6361/201322489)
- Díaz-Santos, T., Armus, L., Charmandaris, V., et al. 2013, *ApJ*, 774, 68, doi: [10.1088/0004-637X/774/1/68](https://doi.org/10.1088/0004-637X/774/1/68)
- . 2017, *ApJ*, 846, 32, doi: [10.3847/1538-4357/aa81d7](https://doi.org/10.3847/1538-4357/aa81d7)
- Farrah, D., Lebouteiller, V., Spoon, H. W. W., et al. 2013, *ApJ*, 776, 38, doi: [10.1088/0004-637X/776/1/38](https://doi.org/10.1088/0004-637X/776/1/38)
- Federrath, C., Klessen, R. S., & Schmidt, W. 2008, *ApJL*, 688, L79, doi: [10.1086/595280](https://doi.org/10.1086/595280)
- Ferland, G. J., Chatzikos, M., Guzmán, F., et al. 2017, *RMxAA*, 53, 385. <https://arxiv.org/abs/1705.10877>
- Foreman-Mackey, D., Sick, J., & Johnson, B. 2014, *python-fsps: Python bindings to FSPS (v0.1.1)*, v0.1.1, Zenodo, doi: [10.5281/zenodo.12157](https://doi.org/10.5281/zenodo.12157)
- Girichidis, P., Konstandin, L., Whitworth, A. P., & Klessen, R. S. 2014, *ApJ*, 781, 91, doi: [10.1088/0004-637X/781/2/91](https://doi.org/10.1088/0004-637X/781/2/91)
- Gnedin, N. Y., Kravtsov, A. V., & Chen, H.-W. 2008, *ApJ*, 672, 765, doi: [10.1086/524007](https://doi.org/10.1086/524007)
- Gnedin, N. Y., Tassis, K., & Kravtsov, A. V. 2009, *ApJ*, 697, 55, doi: [10.1088/0004-637X/697/1/55](https://doi.org/10.1088/0004-637X/697/1/55)
- Goldsmith, P. F., Langer, W. D., Pineda, J. L., & Velusamy, T. 2012, *ApJS*, 203, 13, doi: [10.1088/0067-0049/203/1/13](https://doi.org/10.1088/0067-0049/203/1/13)
- Habing, H. J. 1968, *BAN*, 19, 421
- Harris, C. R., Millman, J., van der Walt, S. J., et al. 2020, *Nature*, doi: [10.1038/s41586-020-2649-2](https://doi.org/10.1038/s41586-020-2649-2)
- Herrera-Camus, R., Bolatto, A., Smith, J. D., et al. 2016, *ApJ*, 826, 175, doi: [10.3847/0004-637X/826/2/175](https://doi.org/10.3847/0004-637X/826/2/175)
- Hewitt, J. W., & Yusef-Zadeh, F. 2009, *ApJL*, 694, L16, doi: [10.1088/0004-637X/694/1/L16](https://doi.org/10.1088/0004-637X/694/1/L16)
- Hopkins, P. F. 2015, *MNRAS*, 450, 53, doi: [10.1093/mnras/stv195](https://doi.org/10.1093/mnras/stv195)
- . 2017, arXiv e-prints, arXiv:1712.01294. <https://arxiv.org/abs/1712.01294>
- Hunter, J. D. 2007, *Computing in Science & Engineering*, 9, 90, doi: [10.1109/MCSE.2007.55](https://doi.org/10.1109/MCSE.2007.55)

- Indriolo, N., Geballe, T. R., Oka, T., & McCall, B. J. 2007, *ApJ*, 671, 1736, doi: [10.1086/523036](https://doi.org/10.1086/523036)
- Inoue, S., Yoshida, N., & Yajima, H. 2020, arXiv e-prints, arXiv:2008.12484. <https://arxiv.org/abs/2008.12484>
- Jones, A. P., Köhler, M., Ysard, N., Bocchio, M., & Verstraete, L. 2017, *A&A*, 602, A46, doi: [10.1051/0004-6361/201630225](https://doi.org/10.1051/0004-6361/201630225)
- Kainulainen, J., Beuther, H., Henning, T., & Plume, R. 2009, *A&A*, 508, L35, doi: [10.1051/0004-6361/200913605](https://doi.org/10.1051/0004-6361/200913605)
- Kamenetzky, J., Rangwala, N., Glenn, J., Maloney, P. R., & Conley, A. 2016, *ApJ*, 829, 93, doi: [10.3847/0004-637X/829/2/93](https://doi.org/10.3847/0004-637X/829/2/93)
- Katsianis, A., Xu, H., Yang, X., et al. 2020, *MNRAS*, doi: [10.1093/mnras/staa3236](https://doi.org/10.1093/mnras/staa3236)
- Kennicutt, Robert C., J. 1998, *ARA&A*, 36, 189, doi: [10.1146/annurev.astro.36.1.189](https://doi.org/10.1146/annurev.astro.36.1.189)
- Kessler, M. F., Steinz, J. A., Anderegg, M. E., et al. 1996, *A&A*, 500, 493
- Kim, C.-G., & Ostriker, E. C. 2017, *ApJ*, 846, 133, doi: [10.3847/1538-4357/aa8599](https://doi.org/10.3847/1538-4357/aa8599)
- Klessen, R. S. 2000, *ApJ*, 535, 869, doi: [10.1086/308854](https://doi.org/10.1086/308854)
- Kroupa, P. 2001, *MNRAS*, 322, 231, doi: [10.1046/j.1365-8711.2001.04022.x](https://doi.org/10.1046/j.1365-8711.2001.04022.x)
- Krumholz, M. R., & Gnedin, N. Y. 2011, *ApJ*, 729, 36, doi: [10.1088/0004-637X/729/1/36](https://doi.org/10.1088/0004-637X/729/1/36)
- Leitherer, C., Ekström, S., Meynet, G., et al. 2014, *The Astrophysical Journal Supplement Series*, 212, 14, doi: [10.1088/0067-0049/212/1/14](https://doi.org/10.1088/0067-0049/212/1/14)
- Leroy, A. K., Walter, F., Brinks, E., et al. 2008, *AJ*, 136, 2782, doi: [10.1088/0004-6256/136/6/2782](https://doi.org/10.1088/0004-6256/136/6/2782)
- Leroy, A. K., Walter, F., Bigiel, F., et al. 2009, *AJ*, 137, 4670, doi: [10.1088/0004-6256/137/6/4670](https://doi.org/10.1088/0004-6256/137/6/4670)
- Leroy, A. K., Usero, A., Schrubba, A., et al. 2017, *ApJ*, 835, 217, doi: [10.3847/1538-4357/835/2/217](https://doi.org/10.3847/1538-4357/835/2/217)
- Leung, T. K. D., Olsen, K. P., Somerville, R. S., et al. 2020, arXiv e-prints, arXiv:2004.11912. <https://arxiv.org/abs/2004.11912>
- Li, Q., Narayanan, D., & Davé, R. 2019, *MNRAS*, 490, 1425, doi: [10.1093/mnras/stz2684](https://doi.org/10.1093/mnras/stz2684)
- Li, Q., Narayanan, D., Davé, R., & Krumholz, M. R. 2018, *ApJ*, 869, 73, doi: [10.3847/1538-4357/aaec77](https://doi.org/10.3847/1538-4357/aaec77)
- Lombardi, M., Alves, J., & Lada, C. J. 2015, *A&A*, 576, L1, doi: [10.1051/0004-6361/201525650](https://doi.org/10.1051/0004-6361/201525650)
- Lord, S. D., Hollenbach, D. J., Haas, M. R., et al. 1996, *ApJ*, 465, 703, doi: [10.1086/177455](https://doi.org/10.1086/177455)
- Lower, S., Narayanan, D., Leja, J., et al. 2020, *ApJ*, 904, 33, doi: [10.3847/1538-4357/abbfa7](https://doi.org/10.3847/1538-4357/abbfa7)
- Lupi, A., & Bovino, S. 2020, *MNRAS*, 492, 2818, doi: [10.1093/mnras/staa048](https://doi.org/10.1093/mnras/staa048)
- Madden, S. C., Rémy-Ruyer, A., Galametz, M., et al. 2013, *PASP*, 125, 600, doi: [10.1086/671138](https://doi.org/10.1086/671138)
- Maeder, A. 2009, *Physics, Formation and Evolution of Rotating Stars* (Berlin Heidelberg: Springer), doi: [10.1007/978-3-540-76949-1](https://doi.org/10.1007/978-3-540-76949-1)
- Mitchell, P. D., Lacey, C. G., Baugh, C. M., & Cole, S. 2013, *MNRAS*, 435, 87, doi: [10.1093/mnras/stt1280](https://doi.org/10.1093/mnras/stt1280)
- Mocz, P., Burkhardt, B., Hernquist, L., McKee, C. F., & Springel, V. 2017, *ApJ*, 838, 40, doi: [10.3847/1538-4357/aa6475](https://doi.org/10.3847/1538-4357/aa6475)
- Narayanan, D., & Krumholz, M. R. 2014, *MNRAS*, 442, 1411, doi: [10.1093/mnras/stu834](https://doi.org/10.1093/mnras/stu834)
- Narayanan, D., Li, Y., Cox, T. J., et al. 2008, *ApJS*, 174, 13, doi: [10.1086/521776](https://doi.org/10.1086/521776)
- Ocvirk, P., Gillet, N., Shapiro, P. R., et al. 2016, *MNRAS*, 463, 1462, doi: [10.1093/mnras/stw2036](https://doi.org/10.1093/mnras/stw2036)
- Ocvirk, P., Aubert, D., Sorce, J. G., et al. 2020, *MNRAS*, 496, 4087, doi: [10.1093/mnras/staa1266](https://doi.org/10.1093/mnras/staa1266)
- Olsen, K., Greve, T. R., Narayanan, D., et al. 2017, *ApJ*, 846, 105, doi: [10.3847/1538-4357/aa86b4](https://doi.org/10.3847/1538-4357/aa86b4)
- Olsen, K., Pallottini, A., Wofford, A., et al. 2018, *Galaxies*, 6, 100, doi: [10.3390/galaxies6040100](https://doi.org/10.3390/galaxies6040100)
- Olsen, K. P., Greve, T. R., Brinch, C., et al. 2016, *MNRAS*, 457, 3306, doi: [10.1093/mnras/stw162](https://doi.org/10.1093/mnras/stw162)
- Olsen, K. P., Greve, T. R., Narayanan, D., et al. 2015, *ApJ*, 814, 76, doi: [10.1088/0004-637X/814/1/76](https://doi.org/10.1088/0004-637X/814/1/76)
- Padoan, P., Haugbølle, T., Nordlund, Å., & Frimann, S. 2017, *ApJ*, 840, 48, doi: [10.3847/1538-4357/aa6afa](https://doi.org/10.3847/1538-4357/aa6afa)
- Padoan, P., & Nordlund, Å. 2011, *ApJ*, 730, 40, doi: [10.1088/0004-637X/730/1/40](https://doi.org/10.1088/0004-637X/730/1/40)
- Pallottini, A., Ferrara, A., Decataldo, D., et al. 2019, *MNRAS*, 487, 1689, doi: [10.1093/mnras/stz1383](https://doi.org/10.1093/mnras/stz1383)
- Pilbratt, G. L., Riedinger, J. R., Passvogel, T., et al. 2010, *A&A*, 518, L1, doi: [10.1051/0004-6361/201014759](https://doi.org/10.1051/0004-6361/201014759)
- Pillepich, A., Springel, V., Nelson, D., et al. 2018, *MNRAS*, 473, 4077, doi: [10.1093/mnras/stx2656](https://doi.org/10.1093/mnras/stx2656)
- Planck Collaboration, Ade, P. A. R., Aghanim, N., et al. 2016, *A&A*, 594, A13, doi: [10.1051/0004-6361/201525830](https://doi.org/10.1051/0004-6361/201525830)
- Popping, G., Narayanan, D., Somerville, R. S., Faisst, A. L., & Krumholz, M. R. 2019, *MNRAS*, 482, 4906, doi: [10.1093/mnras/sty2969](https://doi.org/10.1093/mnras/sty2969)
- Price-Whelan, A. M., Sipőcz, B. M., Günther, H. M., et al. 2018, *AJ*, 156, 123, doi: [10.3847/1538-3881/aabc4f](https://doi.org/10.3847/1538-3881/aabc4f)
- Rahner, D., Pellegrini, E. W., Glover, S. C. O., & Klessen, R. S. 2017, *MNRAS*, 470, 4453, doi: [10.1093/mnras/stx1532](https://doi.org/10.1093/mnras/stx1532)
- Ramos Padilla, A. F., Wang, L., Ploekinger, S., van der Tak, F. F. S., & Trager, S. 2020, arXiv e-prints, arXiv:2011.13441. <https://arxiv.org/abs/2011.13441>

- Rémy-Ruyer, A., Madden, S. C., Galliano, F., et al. 2015, *A&A*, 582, A121, doi: [10.1051/0004-6361/201526067](https://doi.org/10.1051/0004-6361/201526067)
- Rodríguez Montero, F., Davé, R., Wild, V., Anglés-Alcázar, D., & Narayanan, D. 2019, *MNRAS*, 490, 2139, doi: [10.1093/mnras/stz2580](https://doi.org/10.1093/mnras/stz2580)
- Salim, S., Boquien, M., & Lee, J. C. 2018, *ApJ*, 859, 11, doi: [10.3847/1538-4357/aabf3c](https://doi.org/10.3847/1538-4357/aabf3c)
- Salpeter, E. E. 1955, *ApJ*, 121, 161, doi: [10.1086/145971](https://doi.org/10.1086/145971)
- Savage, B. D., & Sembach, K. R. 1996, *ARA&A*, 34, 279, doi: [10.1146/annurev.astro.34.1.279](https://doi.org/10.1146/annurev.astro.34.1.279)
- Schneider, N., Bontemps, S., Girichidis, P., et al. 2015, *MNRAS*, 453, L41, doi: [10.1093/mnrasl/slv101](https://doi.org/10.1093/mnrasl/slv101)
- Schöier, F. L., van der Tak, F. F. S., van Dishoeck, E. F., & Black, J. H. 2005, *A&A*, 432, 369, doi: [10.1051/0004-6361:20041729](https://doi.org/10.1051/0004-6361:20041729)
- Schruba, A., Leroy, A. K., Walter, F., et al. 2012, *AJ*, 143, 138, doi: [10.1088/0004-6256/143/6/138](https://doi.org/10.1088/0004-6256/143/6/138)
- Sormani, M. C., Tress, R. G., Glover, S. C. O., et al. 2020, *MNRAS*, 497, 5024, doi: [10.1093/mnras/staa1999](https://doi.org/10.1093/mnras/staa1999)
- Speagle, J. S., Steinhardt, C. L., Capak, P. L., & Silverman, J. D. 2014, *ApJS*, 214, 15, doi: [10.1088/0067-0049/214/2/15](https://doi.org/10.1088/0067-0049/214/2/15)
- Springel, V. 2010, *MNRAS*, 401, 791, doi: [10.1111/j.1365-2966.2009.15715.x](https://doi.org/10.1111/j.1365-2966.2009.15715.x)
- Stacey, G. J., Geis, N., Genzel, R., et al. 1991, *ApJ*, 373, 423, doi: [10.1086/170062](https://doi.org/10.1086/170062)
- Sun, J., Leroy, A. K., Schruba, A., et al. 2018, *ApJ*, 860, 172, doi: [10.3847/1538-4357/aac326](https://doi.org/10.3847/1538-4357/aac326)
- Teyssier, R. 2002, *A&A*, 385, 337, doi: [10.1051/0004-6361:20011817](https://doi.org/10.1051/0004-6361:20011817)
- Thomas, N., Davé, R., Anglés-Alcázar, D., & Jarvis, M. 2019, *MNRAS*, 487, 5764, doi: [10.1093/mnras/stz1703](https://doi.org/10.1093/mnras/stz1703)
- Thompson, R. 2015, SPHGR: Smoothed-Particle Hydrodynamics Galaxy Reduction. <http://ascl.net/1502.012>
- Tress, R. G., Smith, R. J., Sormani, M. C., et al. 2020, *MNRAS*, 492, 2973, doi: [10.1093/mnras/stz3600](https://doi.org/10.1093/mnras/stz3600)
- Turk, M. J., Smith, B. D., Oishi, J. S., et al. 2011, *The Astrophysical Journal Supplement Series*, 192, 9, doi: [10.1088/0067-0049/192/1/9](https://doi.org/10.1088/0067-0049/192/1/9)
- Vallini, L., Tielens, A. G. G. M., Pallottini, A., et al. 2019, *MNRAS*, 490, 4502, doi: [10.1093/mnras/stz2837](https://doi.org/10.1093/mnras/stz2837)
- Virtanen, P., Gommers, R., Oliphant, T. E., et al. 2020, *Nature Methods*, 17, 261, doi: <https://doi.org/10.1038/s41592-019-0686-2>
- Watson, D. M., Genzel, R., Townes, C. H., Werner, M. W., & Storey, J. W. V. 1984, *ApJL*, 279, L1, doi: [10.1086/184242](https://doi.org/10.1086/184242)
- Weinberger, R., Springel, V., & Pakmor, R. 2020, *ApJS*, 248, 32, doi: [10.3847/1538-4365/ab908c](https://doi.org/10.3847/1538-4365/ab908c)
- Weinberger, R., Springel, V., Hernquist, L., et al. 2017, *MNRAS*, 465, 3291, doi: [10.1093/mnras/stw2944](https://doi.org/10.1093/mnras/stw2944)
- Wes McKinney. 2010, in *Proceedings of the 9th Python in Science Conference*, ed. Stéfan van der Walt & Jarrod Millman, 56 – 61, doi: [10.25080/Majora-92bf1922-00a](https://doi.org/10.25080/Majora-92bf1922-00a)
- Wu, X., Kannan, R., Marinacci, F., Vogelsberger, M., & Hernquist, L. 2019, *MNRAS*, 488, 419, doi: [10.1093/mnras/stz1726](https://doi.org/10.1093/mnras/stz1726)
- Yungelson, L. R., van den Heuvel, E. P. J., Vink, J. S., Portegies Zwart, S. F., & de Koter, A. 2008, *A&A*, 477, 223, doi: [10.1051/0004-6361:20078345](https://doi.org/10.1051/0004-6361:20078345)
- Zhao, Y., Lu, N., Xu, C. K., et al. 2016, *ApJ*, 819, 69, doi: [10.3847/0004-637X/819/1/69](https://doi.org/10.3847/0004-637X/819/1/69)

APPENDIX

A. PROPERTIES OF SIMBA-100 MODEL GALAXY SAMPLE

Table 4 lists the physical properties of the SIMBA-100 galaxy sample while Table 5 lists their line luminosities, including a few ($L_{[\text{OI}]145}$, $L_{[\text{CI}]610}$ and $L_{[\text{CI}]371}$) not used in the validation of the method.

Table 4. Physical properties of the sample of 400 SIMBA-100 galaxies used in this work. A full version of this table is available online.

Galaxy	M_*	M_{gas}	SFR	$\langle Z \rangle_{\text{SFR}}$	$\langle Z \rangle_{\text{mw}}$
index	[$10^{10} M_\odot$]	[$10^{10} M_\odot$]	[$M_\odot \text{ yr}^{-1}$]	[Z_\odot]	[Z_\odot]
0	0.0415	0.6653	0.35	0.16	0.02
1	0.0459	0.7686	0.37	0.10	0.03
2	0.0492	0.6191	0.18	0.12	0.05
3	0.0500	0.9535	0.18	0.13	0.02
4	0.0532	0.8681	0.38	0.16	0.04
5	0.0534	0.6343	0.35	0.14	0.05
6	0.0541	1.0024	0.54	0.15	0.04
7	0.0556	0.7015	0.17	0.15	0.03
8	0.0565	0.6324	0.52	0.11	0.02
9	0.0595	0.5862	0.69	0.15	0.06
10	0.0618	0.9894	0.55	0.17	0.04
11	0.0621	0.6317	0.55	0.14	0.07
12	0.0643	0.7573	0.53	0.14	0.03
13	0.0650	0.7082	0.18	0.14	0.06
14	0.0660	1.0680	0.36	0.19	0.05
15	0.0698	0.9691	0.54	0.16	0.05
16	0.0703	0.6174	0.37	0.16	0.05
17	0.0708	0.9082	0.35	0.18	0.04
18	0.0716	0.9648	0.17	0.20	0.04
19	0.0721	0.6205	0.72	0.10	0.08
20	0.0727	1.1279	0.89	0.19	0.05

Table 5. Line luminosities for the sample of 400 SIMBA-100 galaxies used in this work. A full version of this table is available online.

Galaxy index	$L_{[\text{CII}]158}$	$L_{[\text{CII}]610}$	$L_{[\text{CII}]371}$	$L_{[\text{NII}]205}$	$L_{[\text{NII}]122}$	$L_{[\text{OII}]63}$	$L_{[\text{OII}]145}$	$L_{[\text{OIII}]ss}$	$L_{\text{CO}(1-0)}$	$L_{\text{CO}(2-1)}$	$L_{\text{CO}(3-2)}$
	[L_{\odot}]	[L_{\odot}]	[L_{\odot}]	[L_{\odot}]	[L_{\odot}]	[L_{\odot}]	[L_{\odot}]				
0	2.77e+07	1.21e+05	7.67e+05	5.59e+06	8.55e+06	4.52e+06	9.88e+07	9.87e+05	3.58e+00	1.02e+02	6.68e+02
1	7.40e+07	8.90e+04	7.49e+05	1.72e+07	3.94e+07	1.64e+07	3.72e+08	8.65e+06	1.56e-01	4.87e+00	3.55e+01
2	7.27e+07	2.16e+05	1.59e+06	1.35e+07	2.08e+07	1.75e+07	3.89e+08	2.22e+06	1.48e+01	4.02e+02	2.57e+03
3	4.87e+07	1.85e+05	1.28e+06	9.48e+06	1.31e+07	7.63e+06	1.64e+08	8.45e+05	8.04e+00	2.34e+02	1.58e+03
4	1.13e+08	1.24e+05	1.06e+06	2.55e+07	6.34e+07	3.75e+07	8.92e+08	2.53e+07	6.98e-02	2.17e+00	1.59e+01
5	1.07e+08	1.27e+05	1.10e+06	2.38e+07	5.20e+07	2.79e+07	6.32e+08	9.38e+06	9.42e-02	2.96e+00	2.19e+01
6	1.02e+08	1.68e+05	1.35e+06	2.19e+07	4.19e+07	2.25e+07	4.96e+08	7.77e+06	1.06e+00	3.28e+01	2.35e+02
7	3.69e+07	1.61e+05	1.05e+06	6.83e+06	8.71e+06	6.02e+06	1.28e+08	5.57e+05	8.40e+00	2.44e+02	1.61e+03
8	5.24e+07	9.91e+04	7.94e+05	1.16e+07	2.10e+07	1.03e+07	2.29e+08	1.96e+06	3.84e-01	1.16e+01	8.15e+01
9	1.31e+08	1.44e+05	1.26e+06	2.79e+07	7.45e+07	5.78e+07	1.41e+09	2.46e+07	1.39e-01	4.27e+00	3.12e+01
10	9.01e+07	1.71e+05	1.31e+06	1.95e+07	3.74e+07	1.95e+07	4.32e+08	8.86e+06	3.47e+00	1.04e+02	7.16e+02
11	1.78e+08	1.64e+05	1.48e+06	3.80e+07	1.27e+08	1.00e+08	2.54e+09	5.55e+07	2.69e-03	8.54e-02	6.41e-01
12	6.85e+07	9.09e+04	7.50e+05	1.59e+07	3.49e+07	1.51e+07	3.42e+08	9.40e+06	2.04e-01	6.34e+00	4.60e+01
13	1.30e+08	1.89e+05	1.60e+06	2.69e+07	5.43e+07	4.24e+07	9.72e+08	9.23e+06	7.16e-01	2.22e+01	1.61e+02
14	1.25e+08	2.25e+05	1.81e+06	2.52e+07	4.47e+07	3.51e+07	7.91e+08	7.39e+06	2.68e+00	7.85e+01	5.26e+02
15	9.21e+07	1.69e+05	1.33e+06	1.91e+07	3.38e+07	1.98e+07	4.32e+08	7.33e+06	1.17e+00	3.61e+01	2.60e+02
16	6.45e+07	9.29e+04	7.55e+05	1.38e+07	2.63e+07	1.50e+07	3.28e+08	5.72e+06	4.74e-01	1.47e+01	1.06e+02
17	9.50e+07	2.06e+05	1.58e+06	1.89e+07	3.23e+07	2.38e+07	5.27e+08	7.33e+06	3.09e+00	9.51e+01	6.81e+02
18	8.07e+07	2.37e+05	1.65e+06	1.50e+07	2.43e+07	2.35e+07	5.29e+08	5.97e+06	9.54e+00	2.84e+02	1.94e+03
19	2.64e+08	2.76e+05	2.50e+06	5.12e+07	2.10e+08	1.92e+08	5.01e+09	1.11e+08	2.80e-03	8.89e-02	6.67e-01

B. CONVERGENCE TESTS WITH SKIRT

SKIRT uses a fixed set of photon packets when iterating for a solution to the radiative transfer problem. We tested SKIRT with different photon packet numbers for one large SIMBA-100 galaxy in particular, namely the one shown in the top row of Figure 3. The resulting total FUV luminosity and FUV flux distribution can be seen in Figure 12 for photon packet sizes of 10^6 , 10^7 , 10^8 and 10^9 . There is only a negligible change in FUV luminosity of 0.24% compared to using the lowest photon packet number, but when looking at the flux distribution it becomes clear that at least 10^7 packets are necessary for a stable result, whereas increasing the number to 10^9 has little effect. We therefore settled on 10^8 photon packets.

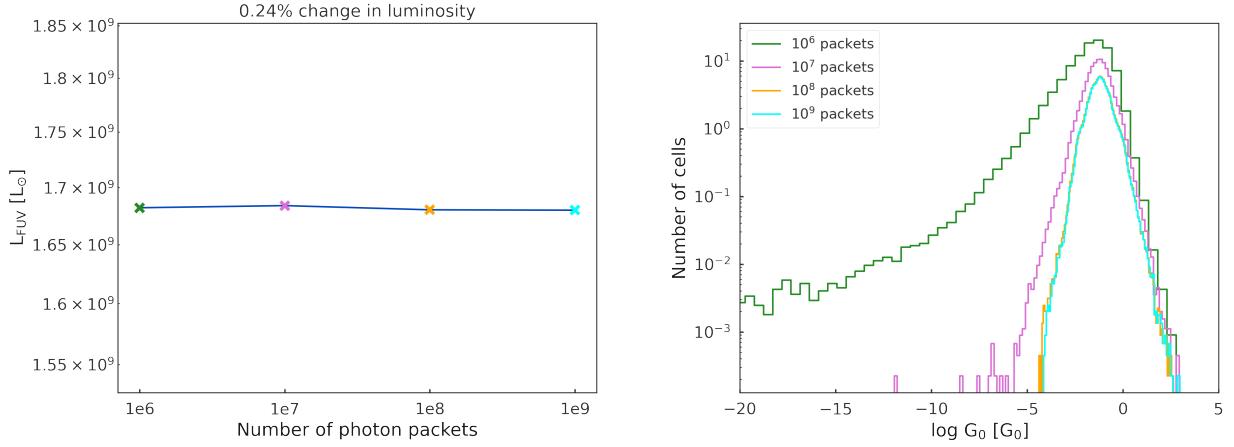


Figure 12. Convergence tests of the SKIRT FUV output for different total numbers of photon packets used in the calculation.

C. DISTRIBUTION OF CELL PHYSICAL PARAMETERS

Figure 13 shows the volume-averaged gas and SFR densities for all cells in all galaxies of our sample. The grid point values in $\langle n_{\text{H}} \rangle_V$ and $\langle n_{\text{SFR}} \rangle_V$ used to sample the CLOUDY grid are also shown in Figure 13. The cells in the SIMBA galaxies have a larger spread in $\langle n_{\text{SFR}} \rangle_V$ and go to lower $\langle n_{\text{H}} \rangle_V$ than the chosen grid points, reflecting a larger parameter space than what is found in AREPO-M51. However, we do not expect this to be a problem since the effect of $\langle n_{\text{SFR}} \rangle_V$ on the density PDF is lesser than that of $\langle n_{\text{H}} \rangle_V$ as seen in Figure 14 and the regions of low $\langle n_{\text{H}} \rangle_V$ are treated separately.

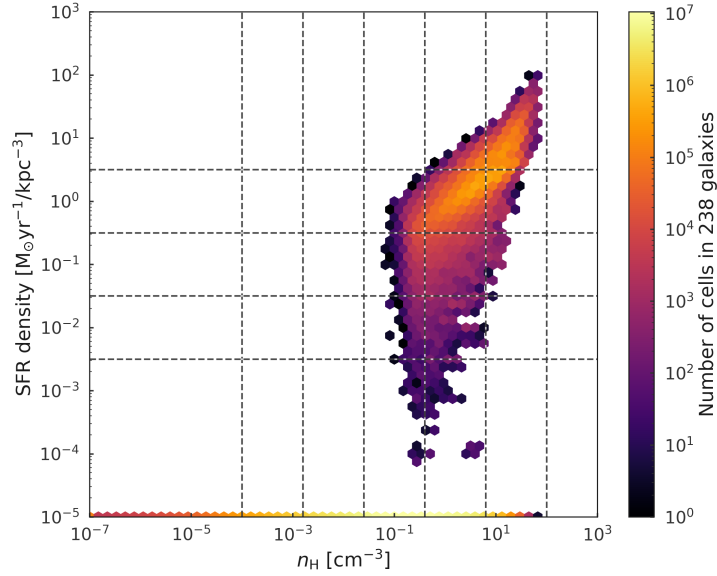


Figure 13. Contour plot showing the cell distribution in density and SFR volume density for all 400 sample galaxies. The horizontal dashed lines indicate the center of the $\langle n_{\text{SFR}} \rangle_V$ bins shown in Figure 14, while the vertical dashed lines correspond to the densities used to sample the SIMBA gas densities in Section 4.4. Cells with $\langle n_{\text{SFR}} \rangle_V = 0 \text{ M}_{\odot} \text{ yr}^{-1} \text{ kpc}^{-3}$ are set to $\langle n_{\text{SFR}} \rangle_V = 10^{-5} \text{ M}_{\odot} \text{ yr}^{-1} \text{ kpc}^{-3}$ in order to show their density distribution in the plot.

D. COMPILATION OF PDFS FROM AREPO-M51

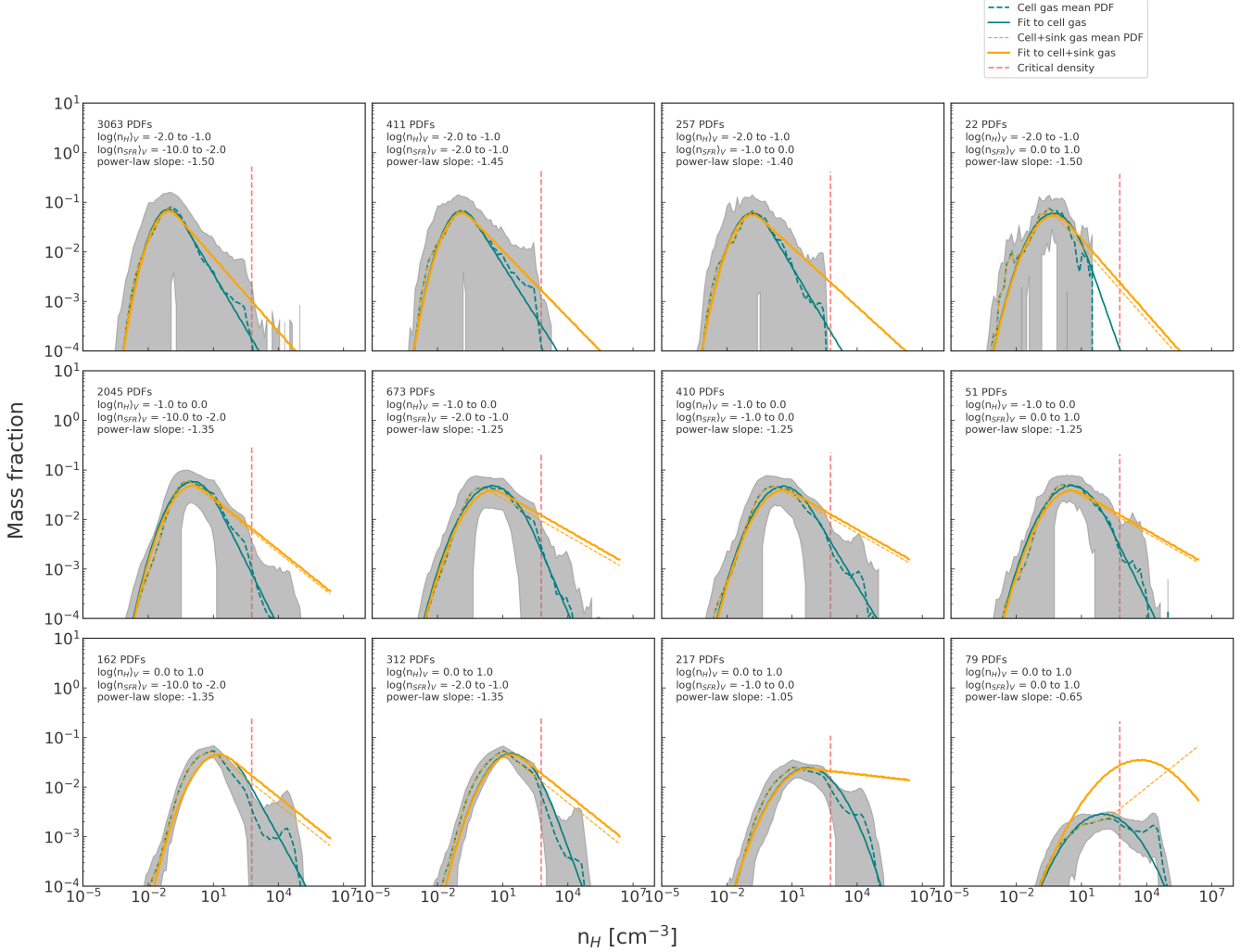


Figure 14. Volume-weighted gas density PDFs from the selected AREPO-M51 run and fitted functions constructed as described in Section 4.3. Each panel indicates a specific bin in gas density, $\langle n_H \rangle_V$, and SFR volume density, $\langle n_{\text{SFR}} \rangle_V$. The grey contours correspond to the $1\text{-}\sigma$ spread around the mean volume-weighted PDF (dashed teal curve) made from AREPO gas cells within regions of $(200\text{ pc})^3$. The solid teal curves are lognormal+power-law fits to the mean PDF. A vertical dashed red line indicates the critical density above which sink particles may form at which point the density PDF from gas cells alone is no longer comprehensive. The orange dashed curves account for the dense gas in sink particles by adding this mass at the high densities in the form of a modified power-law slope, and the orange solid curves are the resulting log-normal+power-law fit to the new distribution. In cases where the modified power-law slope turns positive (last panel), the algorithm is instead allowed to search for a new log-normal center, keeping the power-law slope fixed at -1.5 and deriving the log-normal width.

E. COMPARISON OF SIMILAR GALAXIES IN SIMBA-100 AND SIMBA-25

In order to make a fair comparison of the line emission calculated by *síGAME* for the different SIMBA volumes used here, we have selected a handful of galaxies in both SIMBA-100 and SIMBA-25 that have similar global properties in terms of M_* , M_{gas} , SFR and $\langle Z \rangle_{\text{SFR}}$. We identify “galaxy pairs”, by searching for the smallest distance in the 4D parameter space spanned by the M_* , M_{gas} , SFR and $\langle Z \rangle_{\text{SFR}}$ values, all in log units and normalized to lie in the range from 0 to 1. The result can be seen in Figure 15 in which the luminosity in SIMBA-100 is subtracted from the luminosity in SIMBA-25 for each galaxy pair to give a deviation in luminosity, as function of M_* , M_{gas} , SFR and $\langle Z \rangle_{\text{SFR}}$. The colored lines show the closest pair for the parameter of that panel while the shaded regions show the range in luminosities from the 25th to 75th percentile for all galaxy pairs in that bin. A dashed horizontal line shows a deviation of 0, signalling that both galaxies have equal line luminosity. The vast majority of deviations are within 1 dex, and we attribute the larger deviations at low values of M_* and M_{gas} to the lower mass resolution in SIMBA-100 compared to SIMBA-25. To illustrate the lack in resolution, a vertical dashed line indicates the minimum gas mass in our SIMBA-100 sample with at least 500 gas particles which is $5.6 \times 10^9 M_\odot$. The mass resolution of SIMBA-25 is a factor of 8 higher, with the initial gas particle mass in SIMBA-100 $1.82 \times 10^7 M_\odot$, compared to $2.28 \times 10^6 M_\odot$ in SIMBA-25. Our SIMBA-25 selection contains galaxies with gas masses down to $7.3 \times 10^8 M_\odot$, with the constraint that they contain at least 500 gas particles.

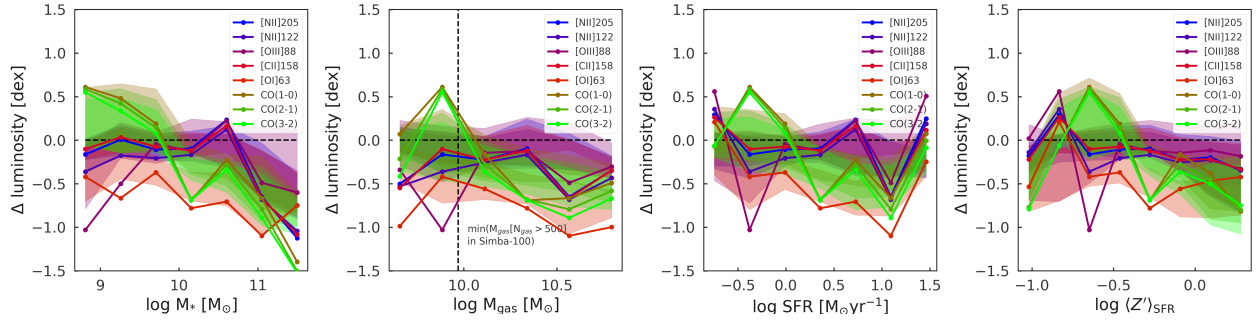


Figure 15. Deviation in line luminosity between galaxies of similar M_* , M_{gas} , SFR and $\langle Z \rangle_{\text{SFR}}$ in SIMBA-100 vs SIMBA-25 as a function of those global properties. Only the eight emission lines considered in this paper are considered, shown here with different colors. Shaded regions show the range in luminosities from the 25th to 75th percentile for all galaxy pairs in that bin.